Mineralium Deposita (2022) 57:1023–1046
https://doi.org/10.1007/s00126-021-01077-w

ARTICLE

Constraints on the structural setting, relative timing, and geochemistry of the Fimiston, Hidden Secret, and Oroya gold-telluride lode types, Kalgoorlie gold camp, Western Australia

Jordan A. McDivitt[1] · Steffen G. Hagemann[1] · Nicolas Thébaud[1] · Laure A. J. Martin[2] · Kai Rankenburg[3]

Received: 27 August 2021 / Accepted: 4 September 2021 / Published online: 25 November 2021

Abstract

Late-stage metamorphic (ca. 2.64 Ga) and punctuated magmatic-hydrothermal mineralization models (2.67–2.64 Ga) are proposed for gold mineralization in the Kalgoorlie gold camp (~ 2300 t Au; Archean Yilgarn craton, Western Australia). We present structural, whole-rock geochemical, pyrite trace element, and multiple sulfur isotope data to evaluate these models. Both the Fimiston and Hidden Secret lodes were emplaced in ca. 2675 Ma D_{2b} transtensional settings as releasing bends developed along the Golden Mile and Towns faults, respectively, and are related to the ingress of a H_2O-CO_2-Au-Te-As-S-K-Rb-Ba fluid concomitant with the intrusion of andesitic dikes. In the Hidden Secret orebody, this magmatic-hydrothermal fluid evolved from an early, As-enriched, greenstone-buffered fluid during the formation of disseminated pyrite mineralization ($\delta^{34}S_{pyrite}$ = 3.42 to 3.85‰; $\Delta^{33}S_{pyrite}$ = 0.25 to 0.43‰) to an Ag-Cu-Pb-Sb-Te-Tl-V-Zn–enriched fluid during the development of banded quartz-carbonate-sericite-pyrite veins ($\delta^{34}S_{pyrite}$ = - 10.74 to - 0.17‰; $\Delta^{33}S_{pyrite}$ = 0.06 to 0.19‰). Oroya gold-telluride lode mineralization formed during later, ca. 2660 Ma D_{2c} transpression from a V-S–Au-Ag-Hg-Te–enriched magmatic-hydrothermal fluid represented by $\delta^{34}S_{pyrite}$ = - 11.56‰ to - 4.96 and $\Delta^{33}S_{pyrite}$ = 0.08 to 0.17‰. The Fimiston/Hidden Secret and Oroya mineralization events record oxidized magmatic-hydrothermal fluids represented by $\delta^{34}S_{pyrite} \leq 0$‰ and $\Delta^{33}S_{pyrite}$ ~ 0.0 to 0.2‰. These oxidized magmatic-hydrothermal fluids interacted with surrounding wall rock, which lowered fluid fO_2 and buffered $\delta^{34}S_{pyrite}/\Delta^{33}S_{pyrite}$ values to $\delta^{34}S_{pyrite}$ = ~ 1 to 5‰/$\Delta^{33}S_{pyrite}$ = ~ 0.2 to 0.7‰ in greenstone rock environments and to $\delta^{34}S_{pyrite}$ = ~ 1 to 5‰/$\Delta^{33}S_{pyrite}$ = ~ ≤ 0.3‰ and ≥ 0.7‰ in black shale environments. Anomalous $\Delta^{33}S$ values in ore-stage sulfides formed locally due to the incorporation of sulfur during fluid-wall rock interaction. The early, magmatic-hydrothermal Fimiston/Hidden Secret and Oroya gold-telluride lodes differ texturally, geochemically, and mineralogically from the D_3 Mt. Charlotte stockwork veins, which formed subsequent to ca. 2650 Ma and better adhere to a late-stage metamorphic devolatilization model.

Keywords Kalgoorlie · Golden Mile · Structural controls on mineralization · SIMS · LA-ICP-MS

Introduction

The sources of fluids and metals in orogenic gold deposits are controversial, with various models including supra-crustal metamorphic sources (Phillips and Groves 1983; Groves and Phillips 1987; Phillips and Powell 2010; Tomkins 2010; Large et al. 2011; Goldfarb and Groves 2015; Selvaraja et al. 2017; Laflamme et al. 2018), sub-crustal, oceanic slab- and sedimentary wedge-derived sources (Goldfarb and Groves 2015; Groves et al. 2020), mantle sources (Colvine et al. 1988; Cameron 1988; Hronsky et al. 2012), intrusion-related sources (Gustafson and Miller, 1937; Mueller et al., 1988; Cameron and Hattori 1987; Burrows and Spooner 1987; Clout 1989; Spooner 1993; Robert 2001; Bateman and

Editorial handling: B. Lehmann.

✉ Jordan A. McDivitt
jordan.mcdivitt@research.uwa.edu.au

[1] Centre for Exploration Targeting, School of Earth Sciences, University of Western Australia, 35 Stirling Highway, Crawley, WA 6009, Australia

[2] Centre for Microscopy, Characterisation, and Analysis, University of Western Australia, 35 Stirling Highway, Crawley, WA 6009, Australia

[3] School of Earth and Planetary Science, John de Laeter Center, Curtin University, Perth, WA 6845, Australia

Hagemann 2004; Mueller 2007; Ispolatov et al, 2008; Kendrick et al. 2011; Xue et al. 2013; Mueller and Muhling 2013; Doublier et al. 2014; Mueller and Muhling 2020; Mueller et al. 2020a), and a combination of the above (Kerr et al. 2018; McDivitt et al. 2018; Thébaud et al. 2018; Masurel et al. 2019; McDivitt et al. 2020) proposed. A key issue fueling the controversy is the presence or absence of multiple mineralization events and how far in time these events are spaced. For example, the presence of a singular, late-stage gold mineralization event is compatible with conventional metamorphic devolatilization models (i.e., Phillips and Groves 1983; Groves and Phillips 1987; Phillips and Powell 2010) and similarly more recent models that invoke sub-crustal, oceanic slab- and sedimentary wedge-derived fluids (Goldfarb and Groves 2015; Groves et al. 2020). The presence of multiple mineralization events that differ in their structural and metamorphic timings are more difficult to reconcile with the aforementioned models, as they implicate multiple fluid events which potentially differ in their genesis and thus are not as easily explained by a singular, late-stage metamorphic devolatilization event (e.g., McCuaig et al. 2001; Robert et al. 2005; Bateman et al. 2008; Dubé et al. 2017; McDivitt et al. 2017, 2018; Kerr et al. 2018; Thébaud et al. 2018, 2020; Masurel et al. 2019). In some cases, the term "broadly synchronous" has been applied to reconcile the presence of multiple mineralization events with a singular, late-stage metamorphic devolatilization event (e.g., Vielreicher et al. 2010, 2016). However, there is an issue with this reconciliation as studies suggest that the multiple mineralization events may be punctuated over 10s of Ma (Bateman and Hagemann 2004; Robert et al. 2005; Dubé et al. 2017; Thébaud et al. 2018; Mueller et al., 2020b), which disfavors the formation of multiple mineralization events due to a singular, late-stage metamorphic devolatilization event. This is further complicated by the interpretative nature of geochronological data, namely, the consideration of geochronological ages as primary, inherited, or reset (e.g., Robert et al. 2005; McDivitt et al. 2020). What may be considered a primary age by one worker may be interpreted as an inherited or reset age by another, leading to various interpretations in the absolute timing of mineralization (e.g., Vielreicher et al. 2015a, b; Bateman and Jones 2015).

Gold mineralization in the Kalgoorlie gold camp (~2300 t Au; Yilgarn craton, Western Australia; McDivitt et al. 2020) is considered a type example of orogenic gold mineralization (Hagemann and Cassidy 2000). The immense endowment of the camp has led to the proposition that it records the optimization of typical orogenic ore-forming processes associated with late-stage, metamorphic devolatilization of supra-crustal or sub-crustal volcano-sedimentary successions (Phillips 1986; Phillips et al. 1987, 1996; Groves et al. 2016; Vielreicher et al. 2016). Although mineralization in the camp is considered archetypal orogenic mineralization, the controversies and difficulties outlined in the preceding paragraph are well-exemplified. For example, the different mineralization types in the camp (Fimiston, Hidden Secret, Oroya, Mt. Charlotte) are considered by some workers to be broadly synchronous at ca. 2.64 Ga (Vielreicher et al. 2010, 2016) and by others to have formed via punctuated mineralization events from ca. 2.67 to 2.64 Ga (Bateman and Hagemann 2004; Robert et al. 2005; Mueller 2020a). Those that prefer broadly synchronous mineralization at ca. 2.64 Ga tend to invoke metamorphic fluids in the formation of mineralization (Vielreicher et al. 2010, 2016). In contrast, those that favor punctuated mineralization from ca. 2.67 to 2.64 Ga suggest magmatic-hydrothermal fluid models for the Fimiston and Oroya mineralization types (Mueller et al., 1988; Clout 1989; Bateman and Hagemann 2004; Mueller 2007; Mueller and Muhling 2013; Mueller and Muhling 2020; Mueller et al. 2020a). The geochemical data from the different mineralization types is variably interpreted to record a broadly synchronous hydrothermal system (Vielreicher et al. 2016) or to record multiple punctuated hydrothermal systems (Bateman et al. 2001a; McDivitt et al. 2020). Therefore, the Kalgoorlie gold camp provides an excellent setting to provide insight into key issues fuelling controversy for genetic and timing models in orogenic gold systems. For this purpose, we present new structural and geochemical data (hydrothermal alteration mass balance, LA-ICP-MS and SIMS for trace elements and multiple sulfur isotopes in pyrite, respectively) for the well-characterized Fimiston and Oroya gold-telluride lode mineralization types as well as the poorly characterized Hidden Secret gold-telluride lode mineralization type from the newly discovered lower Hidden Secret orebody. The Hidden Secret gold-telluride lodes have not been studied in the same detail as the other mineralization types in this camp, and their structural timing, geochemical nature, and relationship to other mineralization types are largely unconstrained. Additionally, most samples of Oroya mineralization that have been studied in detail come from the Oroya shoot area in the Paringa South mine (e.g., Radtke 1963; Godefroy-Rodríguez et al., 2020a; Godefroy-Rodríguez et al., 2020b; Mueller 2020b; Mueller et al. 2020a), proximal to the Oroya Shale interflow sedimentary rock horizon, with the latter interpreted to have a significant influence on the geochemistry of mineralization (Mueller et al. 2020a). Access to the newly discovered underground Hidden Secret orebody as well as Oroya mineralization recently exposed at depth in the Golden Mile Super Pit, distal from the Oroya shoot area, provides new evidence for the punctuated or synchronous nature of mineralization in the Golden Mile and constrains genetic models for the broader orogenic gold deposit class. Furthermore, the ability of geochemical data to discriminate different mineralization events, fingerprint genetic processes, and constrain the source components of gold mineralization in orogenic gold

deposits is scrutinized by this study, with cautionary aspects regarding the use of the $\Delta^{33}S$ parameter emphasized.

Geologic setting and gold mineralization

Geologic setting

Gold deposits of the Kalgoorlie gold camp (Fig. 1A) comprise the super-giant Golden Mile Super Pit (~ 1780 t Au produced), which hosts the high-grade Oroya shoot (> 62 t Au produced), as well as the Mt. Charlotte (~ 155 t Au produced), Mt. Percy (~ 8 t Au produced), and Hidden Secret (~ 2.4 t Au) orebodies (Mueller 2015, 2020a; McDivitt et al. 2020). The deposits are exposed in a window of Kambalda Sequence stratigraphy through the overlying Kalgoorlie Sequence (Fig. 1B; Hand 1998; Krapež et al. 2000; Krapež and Hand 2008), where ultramafic and mafic dolerite sills have intruded the volcano-sedimentary pile. These include the 2685 ± 4 Ma (2σ) Golden Mile Dolerite (U–Pb SHRIMP zircon; Tripp 2013), the 2696 ± 5 Ma (2σ) Williamstown Dolerite (U–Pb SHRIMP zircon; Fletcher et al. 2001), and the undated Aberdare, Federal, and Eureka dolerites (Clout 1989; Bateman et al. 2001b). From oldest to youngest, Kambalda Sequence stratigraphy comprises the Hannan Lake Serpentinite (2708 ± 7 Ma (2σ); U–Pb SHRIMP zircon; Nelson 1997), the Devon Consols Basalt, the Kapai Slate (2692 ± 4 Ma (2σ); U–Pb SHRIMP zircon; Claoué-Long et al. 1988), and the Pargina Basalt. The upper termination of the Kambalda Sequence is marked locally by the Oroya Shale horizon and tholeiitic basalts of the Lower Black Flag Group (Fig. 1B; Clout et al. 1990; Bateman et al. 2001b; Mueller et al. 2020b). The latter comprises ca. 2690–2680 Ma volcanic sandstone, siltstone, and sulfide-rich black shale (Squire et al. 2010; Mueller 2015; Mueller et al. 2020b) and demarcates the transition to the Kalgoorlie Sequence. The Kalgoorlie Sequence consists of Lower and Upper Black Flag Groups, with the boundary between the Lower and Upper Black Flag Groups represented by the Gidji Lake unconformity (Tripp 2013, 2014). The Upper Black Flag Group comprises turbididic mudstones, siltstones, sandstones, tuff, agglomerate, and intermediate to felsic volcanic flow rocks (Woodall 1965; Eaton 1986; Clout et al. 1990). Late-stage porphyry dikes cross-cut the Golden Mile Dolerite and Lower Black Flag Group in the Golden Mile Super Pit (Fig. 2A–C). These dikes include ca. 2675 Ma (U–Pb SHRIMP zircon), leucocratic, quartz-feldspar-phyric porphyries as well as mesocratic, hornblende-phyric porphyries and melanocratic lamprophyres, with the latter two dike types interpreted to have been emplaced from ca. 2675 to 2640 Ma (U–Pb SHRIMP zircon; Woods 1997; Yeats et al. 1999; Gauthier et al. 2004; McNaughton et al. 2005; Vielreicher et al. 2010).

Various deformation schemes for the camp (i.e., Mueller et al. 1988; Swager 1989; Bateman and Hagemann 2004; Weinberg et al. 2005; Mueller 2015, 2020a) have been summarized and re-interpreted in McDivitt et al. (2020) and integrated with local and regional geochronological constrains on the timing of deformation provided by Krapež et al. (2000), Fletcher et al. (2001), Ross et al. (2004), Gauthier et al. (2004), Mueller (2007), Tripp (2013), and Mueller et al. (2020b). Further work by McDivitt et al. (2021a) refines the deformation history of the camp as follows: early D_1 fold-and-thrust-type deformation, when structures such as the Golden Mile fault zone and Kalgoorlie anticline (Fig. 1A) formed, is constrained with a maximum age of 2684 ± 5 Ma (2σ; U–Pb SHRIMP zircon; Tripp 2013) and a minimum age of 2680 ± 3 Ma (2σ; U–Pb SHRIMP zircon; McDivitt et al. 2021a). Regional D_2 sinistral transpression from ca. 2675 to 2655 Ma (McDivitt et al. 2020) is subdivided locally into the following (McDivitt et al. 2021a): D_{2a} sinistral strike-slip at 2680 ± 3 Ma (2σ; U–Pb SHRIMP zircon; McDivitt et al. 2021a); D_{2b} sinistral transtension at ca. 2675 Ma; and D_{2c} sinistral-reverse deformation at ca. 2660 Ma. Late, N- to NNE-tending D_3 dextral faults formed from ca. 2650 to 2640 Ma.

Gold mineralization

Fimiston lodes are preferentially NW-striking, steeply dipping (ESM Fig. 1A) banded, brecciated, colloform, and crustiform carbonate-quartz vein zones with sulfides (predominantly pyrite), sulfosalts (tennantite-tetrahedrite ± enargite), magnetite, hematite, telluride minerals, and native gold (Clout et al. 1990; Mueller 2007; Godefroy-Rodríguez et al., 2020a; Mueller, 2020a). They are surrounded by proximal and distal alteration zones comprising sericite-ankerite-siderite-quartz-hematite-pyrite-telluride and ankerite-sericite-quartz-pyrite, respectively (Clout et al. 1990; Bateman and Hagemann 2004). The lodes are deformed by a NNW-striking sub-vertical cleavage (ESM Fig. 1B; Gauthier et al. 2004; McDivitt et al. 2020) and sub-divided on the basis of their orientation (Fig. 2B) into Main lodes (140/60–75; 150/90), Caunter lodes (120/70–60; 104/80–60), and Cross lodes (026/90) (Travis et al. 1971; Bateman and Hagemann 2004; Mueller 2020a). These various lode orientations are interpreted to record Riedel shear zone-type structures formed during D_2 sinistral transcurrent shearing (Mueller et al. 1988; Mueller 2020a). More recently, it has been suggested that the Fimiston lodes formed within a ca. 2675 Ma D_{2b} sinistral transtensional environment related to the development of a releasing bend during sinistral shearing along the Golden Mile fault zone (McDivitt et al. 2021a).

Mineralization in the Hidden Secret area (Fig. 1A) includes that from the historic upper Hidden Secret orebody (~ 1.2 t Au produced; Feldtmann 1916; Keats 1987;

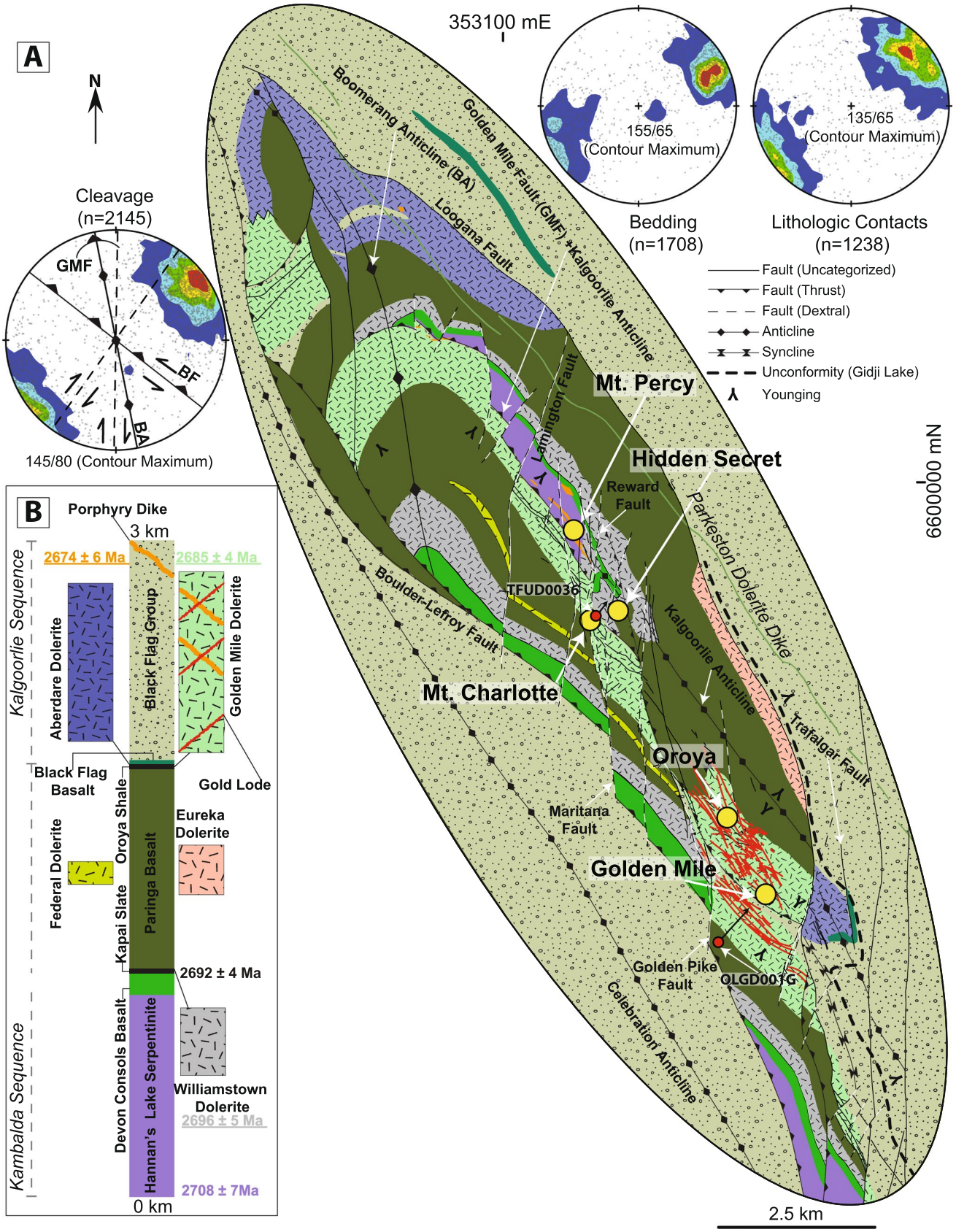
A
N
353100 mE
6600000 mN
Cleavage
(n=2145)
GMF
BF
BA
145/80 (Contour Maximum)
155/65
(Contour Maximum)
Bedding
(n=1708)
135/65
(Contour Maximum)
Lithologic Contacts
(n=1238)
Fault (Uncategorized)
Fault (Thrust)
Fault (Dextral)
Anticline
Syncline
Unconformity (Gidji Lake)
Younging
Boomerang Anticline (BA)
Golden Mile Fault (GMF)
Kalgoorlie Anticline
Loogana Fault
Lamington Fault
Mt. Percy
Hidden Secret
Reward Fault
Parkeston Dolerite Dike
TFUD0036
Boulder-Lefroy Fault
Mt. Charlotte
Kalgoorlie Anticline
Trafalgar Fault
Oroya
Maritana Fault
Golden Mile
Golden Pike Fault
OLGD001G
Celebration Anticline
2.5 km
B
Porphyry Dike
3 km
2674 ± 6 Ma
2685 ± 4 Ma
Kalgoorlie Sequence
Aberdare Dolerite
Black Flag Group
Golden Mile Dolerite
Black Flag Basalt
Gold Lode
Oroya Shale
Eureka Dolerite
Federal Dolerite
Paringa Basalt
Kapai Slate
2692 ± 4 Ma
Devon Consols Basalt
Hannan's Lake Serpentinite
Williamstown Dolerite
2696 ± 5 Ma
Kambalda Sequence
2708 ± 7Ma
0 km

◂**Fig. 1** After McDivitt et al. (2020). **A** Camp-scale geologic map produced from KCGM mapping and compilation. The location of the Gidji Lake Unconformity is from G.I. Tripp (personal communication, 25/07/2019). Gold deposits of the Kalgoorlie gold camp (the Golden Mile, Mt. Charlotte, Hidden Secret, and Mt. Percy deposits) as well as the Oroya shoot are shown as yellow dots. Stereonets (lower hemisphere, equal area) are produced from the KCGM database of oriented drill core and display contoured poles (1% area; start = 2%; contour intervals = 2%) of planar features. Upper left stereonet shows poles to regional cleavage measurements and trends of camp-scale structures such as the Golden Mile fault (GMF), Boulder-Lefroy fault (BF), Boomerang anticline (BA), and late, N- to NNE-tending dextral faults. The upper right stereonets display poles to bedding planes and lithologic contacts. Map coordinates in UTM zone 51 J, WGS84 datum. The thrust kinematics indicated for Boulder-Lefroy fault and other NW- to NNW-striking faults may record late, ENE-WSW bulk shortening superimposed on earlier sinistral strike-slip faults (Mueller et al., 2020b). **B** Scaled stratigraphic column depicting the volcanic, sedimentary, and intrusive rocks of the Kalgoorlie gold camp in the context of geochronological age constraints. Stratigraphic nomenclature after Krapež et al. (2000); reported radiometric ages are U–Pb SHRIMP zircon (2σ) from Claoué-Long et al. (1988), Kent and McDougall (1995), Nelson (1997), Fletcher et al. (2001), and Tripp (2013)

Mueller 2020a) and the newly discovered lower Hidden Secret (~ 2.4 t Au), which is the subject of this study. Hidden Secret-type gold-telluride lode mineralization is located in the lower Hidden Secret orebody at the S-folded contact between the Devon Consols Basalt and the Williamstown Dolerite at the Kapai Slate interflow sedimentary rock horizon on the steeply dipping western limb of the Kalgoorlie anticline, which plunges ~ 20° SE (Fig. 3A, B; Fitzgerald and Nixon 2016). Hidden Secret lodes comprise banded quartz-carbonate-sericite veins containing pyrite, chalcopyrite, galena, sphalerite, pentlandite, sulfosalts, tellurides, and gold surrounded by proximal quartz-carbonate-sericite-fuchsite and distal carbonate-quartz-sericite-chlorite alteration zones (Verbeeten 2014; Sellman 2016). The Hidden Secret lodes differ from the Fimiston lodes by higher hessite (AgTe) and petzite ($AuAg_3Te_3$) and lower calaverite ($AuTe_2$) concentrations, which is reflected geochemically by higher Ag:Au ratios and a stronger Au–Ag correlation in the Hidden Secret lodes (Simpson and Gibson 1912; Keats 1987; Mueller and Muhling 2013; Fitzgerald and Nixon 2016; Sellman 2016; McDivitt et al. 2020). The Hidden Secret lodes are similar in orientation to the Fimiston lodes and are NW-striking and sub-vertical to steeply SW dipping (ESM Fig. 1C), with zones of high-grade ores that plunge ~ 40° to 150°. Like in the Golden Mile, a prominent NNW-striking, sub-vertical cleavage is well-defined in the lower Hidden Secret orebody (ESM Fig. 1D).

Oroya-type mineralization is a gold-telluride lode mineralization type that is best characterized in the Oroya shoot area (Fig. 2A), where shallowly plunging ore shoots occur in proximity to the Oroya Shale horizon at the Golden Mile Dolerite-Paringa Basalt interface. The Oroya shoot plunges 15°–30° SE and is bound by the NW-striking and SW-dipping Oroya hanging wall and footwall D_{2c} thrust faults (Lungan 1986; Mueller et al. 1988; Muller and Muhling 2020); these thrust faults cross-cut and offset earlier D_{2b} Fimiston lode structures (Mueller 2020a). Oroya mineralization is distinguished by deep-green, quartz-sericite-carbonate-pyrite-telluride-nolanite-titanium vanadate-vanadium muscovite Green Leader alteration (Tomich 1958; Nickel 1977; Eaton 1986).

Mt. Charlotte-type stockwork veins are another mineralization type in the camp. They are most prevalent in the Mt. Charlotte area (Fig. 1A; Clark 1980; Clout et al. 1990; Ridley and Mengler 2000; Mueller 2015) where they constitute the Charlotte, Reward, Northern, and Maritana orebodies. The stockwork veins comprise planar quartz-carbonate-sericite-albite-scheelite-sulfide-gold veins (Clark 1980; Clout et al. 1990; Ridley and Mengler 2000; Mueller 2015). The veins occur as steeply NW- or SE-dipping and shallowly to moderately N-dipping sets (ESM Fig. 1E, F; Clout et al. 1990; Ridley and Mengler 2000). The veins are surrounded by yellow-gray (bleached) ankerite-sericite-albite-pyrite-siderite-rutile alteration halos that become increasingly pyrrhotite and albite rich at depth (Clark 1980; Mernagh et al. 2004; Bateman and Hagemann 2004; Mueller 2015). The Mt. Charlotte-type stockwork veins are interpreted to have formed late during D_3 (McDivitt et al. 2021a).

Methods

The analytical methods utilized in this manuscript are outlined in detail in the Electronic Supplementary Material (ESM) Appendix 1. Samples for microscopic, geochemical, and microstructural analysis were collected during lode-scale mapping of the Golden Mile Super Pit, particularly the deep levels below 500 m depth, and the underground Hidden Secret orebody at the 230–430 m reference levels (RLs). Polished thin sections were studied in transmitted and reflected light, and analyzed using backscattered electron imaging (BSE) and energy-dispersive spectroscopy (EDS).

Samples collected from location 2 in the Super Pit (Fig. 2A) for hydrothermal alteration mass balance calculations include Fimiston- and Oroya-altered (proximal) Golden Mile Dolerite (Unit 8) as well as least-altered Golden Mile Dolerite (Unit 8). Additional Fimiston-altered (proximal) Golden Mile Dolerite (Unit 9) and least-altered Golden Mile Dolerite (Unit 9) were collected from DDH OLGD001G (Fig. 1A). In the Hidden Secret area, altered (proximal and distal) and

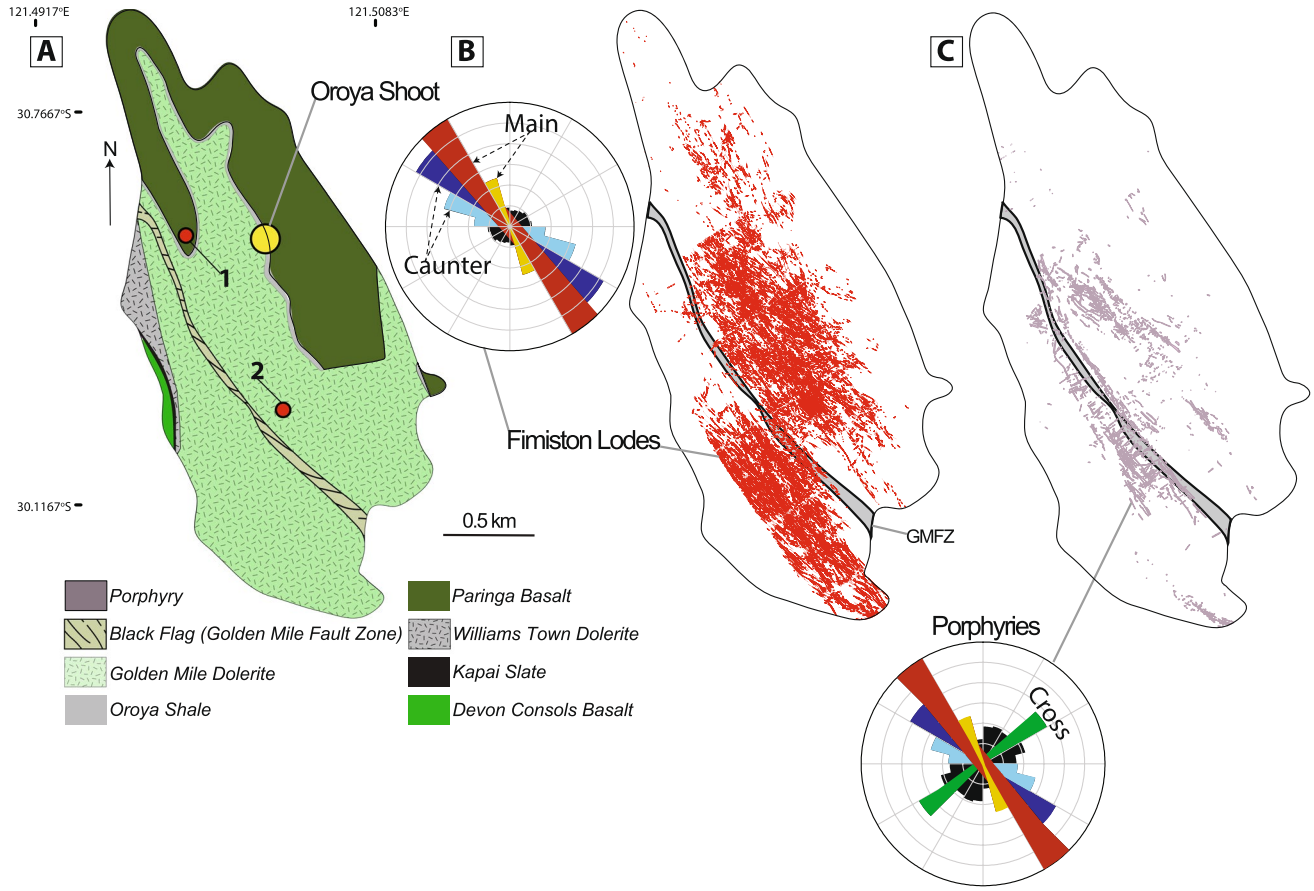

Fig. 2 **A** Geologic map of the Golden Mile Super Pit. The red dots labeled 1 and 2 denote the Fimiston lode exposures documented in this study. **B** The distribution of Fimiston lodes in the Super Pit as recorded by historic underground mapping. The rose diagram displays the relative frequency of different lode orientations as determined by line orientation analysis. **C** The distribution of porphyry intrusions in the Super Pit as recorded by historic underground mapping. The rose diagram displays the relative frequency of different porphyry orientations as determined by line orientation analysis. Figures produced from KCGM mapping and data compilation

least-altered Williamstown Dolerite was collected from DDH TFUD0036 (Fig. 1A), and porphyry dike samples were collected from the underground Hidden Secret orebody. Rock samples were analyzed for whole-rock geochemical data at ALS in Perth. Mass balance calculations utilized the procedures outlined by Grant (1986) and Huston (1993). The results of whole-rock geochemical analysis and mass balance are presented in ESM Appendix 2 and Appendix 3. Samples for laser ablation inductively coupled plasma mass spectrometry (LA-ICP-MS) pyrite trace element analysis were analyzed at the Geo-History Facility, John de Laeter Centre, Curtin University (ESM Appendix 4). Triple sulfur isotope analysis (^{32}S, ^{33}S, ^{34}S) of pyrite was completed on a secondary ion mass spectrometer (SIMS) Cameca 1280 at the Centre for Microscopy Characterisation and Analysis, at the University of Western Australia (ESM Appendix 5).

Results

Structural and relative timing relationships

Super pit At location 1 (Fig. 2A), D_{2b} Fimiston lodes are NW- to WNW-striking, steeply SW- or NNE-dipping, and flanked by narrow, NW- to WNW-striking, steeply SW-dipping marginal veins, which define upward-pointing, acute bifurcations where they intersect the lodes (ESM Fig. 2A). Within the lodes, asymmetric breccia clasts define a D_{2b} normal shear component (ESM Fig. 2B, C). On the lode margins, S_{2b} fabric drag defines a normal shear component (ESM Fig. 2D); sub-horizontal lineations and steps define a sinistral strike-slip shear component (ESM Fig. 2E). Fimiston lode veins include foliated wall rock (ESM Fig. 2F) and define asymmetric folds illustrating both D_{2b} normal and D_{2c} reverse shear components (ESM Fig. 2G). Where asymmetric folds define a D_{2c} reverse shear component, a

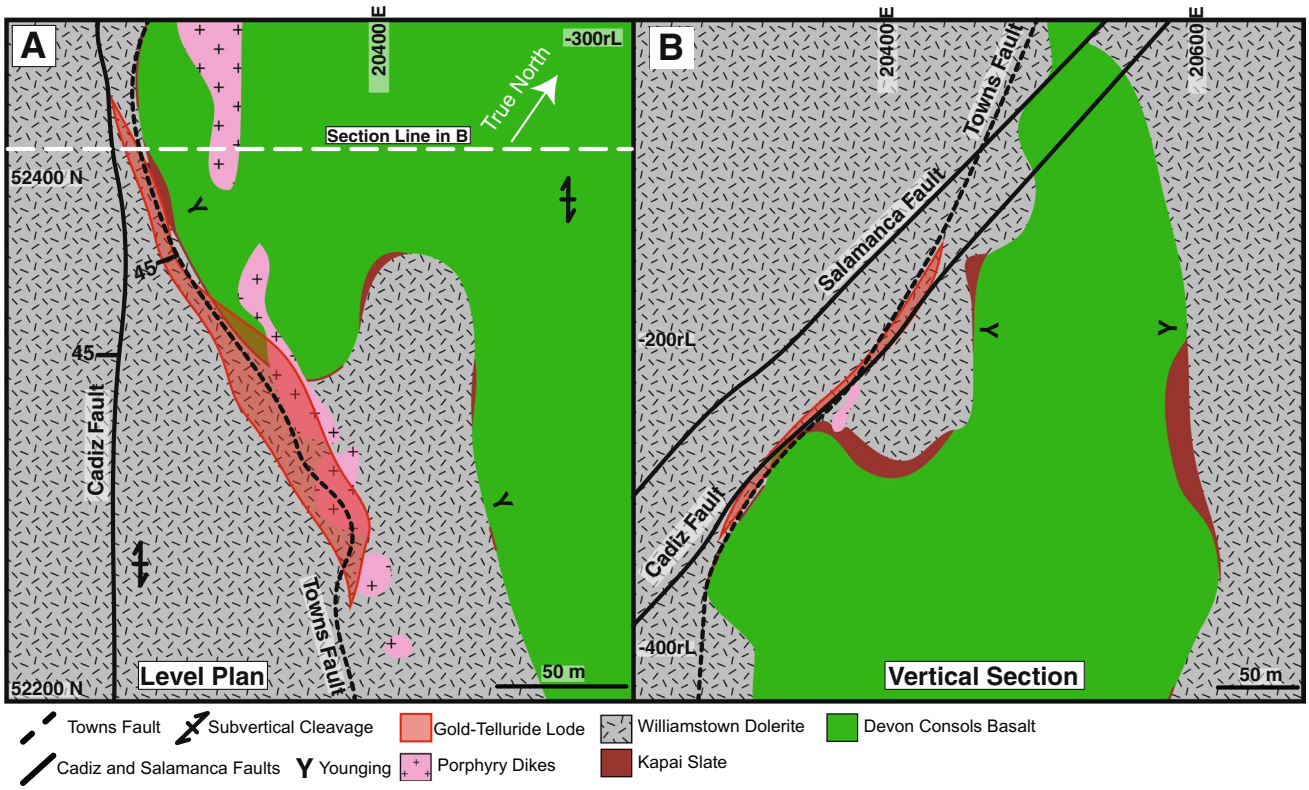

Fig. 3 Geologic plan map (**A**) and cross-section (**B**) of the Hidden Secret orebody. Figures produced from sections provided by the KCGM mine geology team

NW-striking, sub-vertical S_{2C} cleavage is axial planar to the folds (ESM Fig. 3).

At location 2 (Fig. 2A), NW- to WNW-striking, sub-vertical D_{2b} Fimiston lode veins (ESM Fig. 4A, B) are surrounded by proximal albite-sericite-siderite alteration in Golden Mile Dolerite (Fig. 4A, B). Along the lode margins, sub-horizontal slickenlines are developed in association with steps recording sinistral strike-slip shear zone movement (ESM Fig. 4C). Reverse D_{2c} kinematics are defined along the lode margins by $S_{2c}S$ and $S_{2C}C$ fabrics (ESM Fig. 4D). The lodes and the albite-sericite-siderite–altered Golden Mile Dolerite are cross-cut at a high angle by D_{2c} Oroya-type pyritic stringer veins surrounded by dark-colored, sericite-albite-quartz alteration halos (Fig. 4A; ESM Fig. 4A, E).

Hidden secret underground In the 310 m RL south drive, a D_{2b}-banded Hidden Secret vein is hosted in green, carbonate-fuchsite-quartz–altered Williamstown Dolerite and is folded and transected by later D_3 stockwork veins (Fig. 5A). The carbonate-fuchsite-quartz–altered Williamstown Dolerite is intruded by a leucocratic dike, and tan-colored reaction halos are developed around dolerite xenoliths (Fig. 5B). Both the altered dolerite and the dike are cross-cut by a D_{2b}-banded vein, which is in turn cross-cut by a D_3 stockwork vein (Fig. 5B).

In the 290 m RL south drive, a WNW-striking, moderately SW-dipping D_{2b}-banded vein (HS1 vein) and breccia defining a lode are hosted in carbonate-fuchsite-quartz–altered Williamstown Dolerite (Fig. 6A). The HS1 vein is host to hessite included within pyrite (Fig. 6B). A leucocratic dike is located in the hanging wall and footwall of the lode. A WNW-striking, moderately to steeply SW-dipping cleavage is developed in the lode, altered dolerite, and the dike. The cleavage, lode, altered dolerite, and dike are cross-cut by WSW- to SW-striking, sub-vertical to moderately N-dipping D_3 stockwork veins (Fig. 6A). The lode is also cross-cut and offset by a N-striking, steeply W-dipping D_{2b} fault filled with a mesocratic dike (Fig. 6A, C). Laminated veins (HS2 veins) occur along the offset fault and parallel the dike (Fig. 6C); these HS2 veins also host hessite which is intergrown with pyrite (Fig. 6D). The HS2 veins are linked with NW-striking, moderately SW-dipping veins at the margins of the fault, and these marginal veins parallel an S_{2b} cleavage and are dragged along the HS2 veins defining a normal sense of D_{2b} shear movement (Fig. 6C). Later D_{2c} reverse deformation is evidenced by a NW-striking,

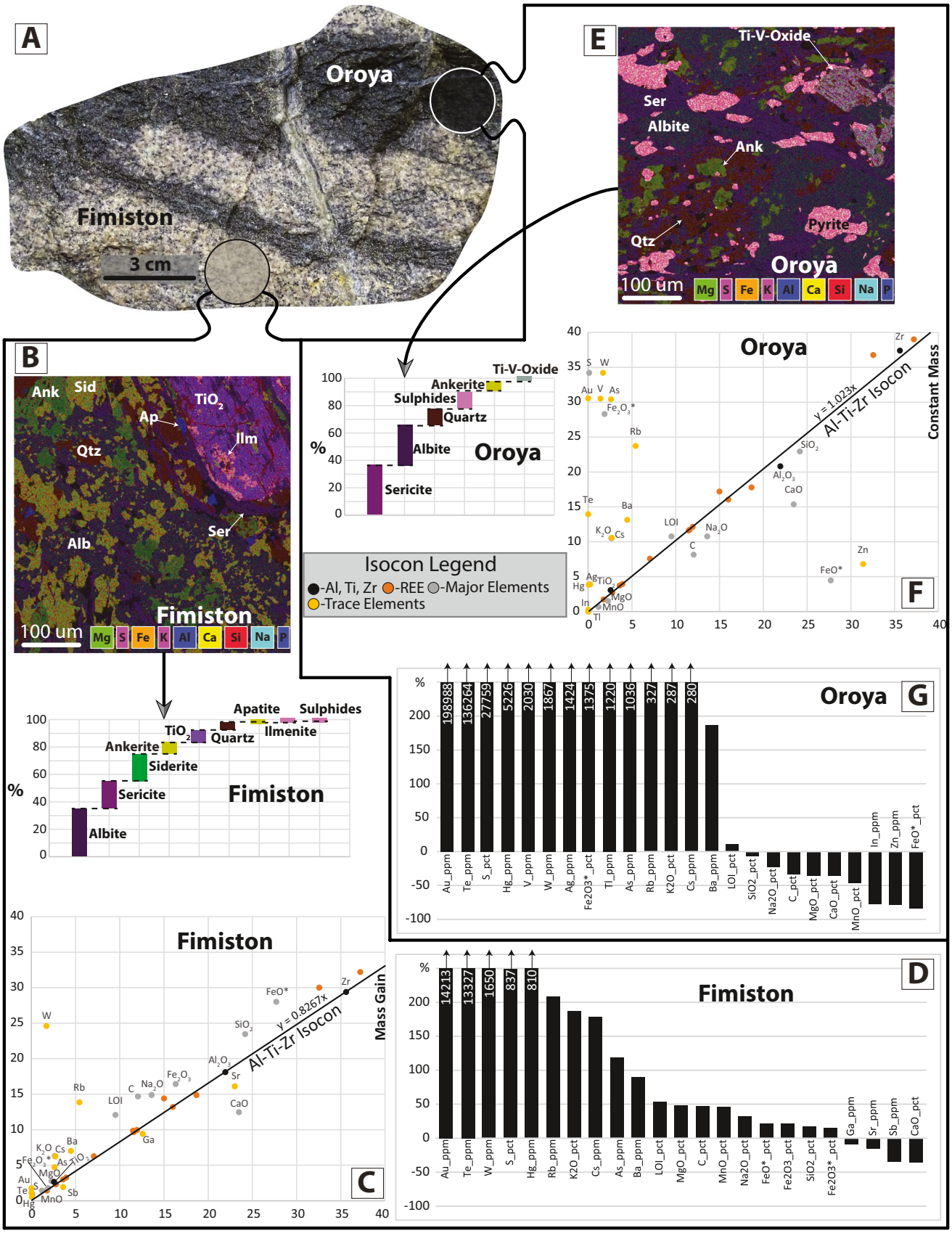
A
Oroya
Fimiston
3 cm
E
Ti-V-Oxide
Ser
Albite
Ank
Pyrite
Qtz
Oroya
100 um
Mg S Fe K Al Ca Si Na P
B
Ank
Sid
TiO2
Ap
Ilm
Qtz
Ser
Alb
Fimiston
100 um
Mg S Fe K Al Ca Si Na P
Ti-V-Oxide
Ankerite
Sulphides
Quartz
Albite
Sericite
Oroya
%
Isocon Legend
-Al, Ti, Zr -REE -Major Elements
-Trace Elements
Oroya
Al-Ti-Zr Isocon
y = 1.023x
Constant Mass
F
Apatite
Sulphides
TiO2
Quartz
Ilmenite
Ankerite
Siderite
Sericite
Albite
Fimiston
%
Oroya
G
198988
136264
27759
5226
2030
1867
1424
1375
1220
1036
327
287
280
Au_ppm
Te_ppm
S_pct
Hg_ppm
V_ppm
W_ppm
Ag_ppm
Fe2O3*_pct
Tl_ppm
As_ppm
Rb_ppm
K2O_pct
Cs_ppm
Ba_ppm
LOI_pct
SiO2_pct
Na2O_pct
C_pct
MgO_pct
CaO_pct
MnO_pct
In_ppm
Zn_ppm
FeO*_pct
Fimiston
Al-Ti-Zr Isocon
y = 0.8267x
Mass Gain
C
Fimiston
D
14213
13327
1650
837
810
Au_ppm
Te_ppm
W_ppm
S_pct
Hg_ppm
Rb_ppm
K2O_pct
Cs_ppm
As_ppm
Ba_ppm
LOI_pct
MgO_pct
C_pct
MnO_pct
Na2O_pct
FeO*_pct
Fe2O3_pct
SiO2_pct
Fe2O3*_pct
Ga_ppm
Sr_ppm
Sb_ppm
CaO_pct

◂**Fig. 4** Fimiston-Oroya relationships from location 2 in the Super Pit and mass balance results. Isocon diagrams use scaled values (Grant 1986). (A) Sample from where sub-vertical Fimiston lode veins are cut at a high angle by the pyritic stringers in ESM Fig. 4. The light-colored areas in the sample correlate to Fimiston alteration developed in the Golden Mile Dolerite. The dark-colored areas represent Oroya alteration which cross-cuts the earlier Fimiston mineralization. Whole-rock geochemical data and mineralogy for these alteration types is given in ESM Appendix 2. Relative changes in element concentrations determined by mass balance calculations are reported in ESM Appendix 3. (B) Mineralogy of the Fimiston alteration zone shown in a false-colored, SEM-BSE-EDS image with modal percentages given on the corresponding graph. Fimiston alteration comprises albite (Alb), sericite (Ser), siderite (Sid), ankerite (Ank), TiO2 mineral, quartz (Qtz), apatite (Ap), ilmenite (Ilm), and sulfide. (C) Isocon diagram illustrating the elemental gains and losses associated with Fimiston alteration. The isocon slope < 1 is indicative of mass gain in the alteration zone. (D) Histogram diagram displaying the elemental changes recorded in Fimiston alteration as percentage change. Gold grades in the least-altered sample and altered sample are 0.003 ppm and 0.355 ppm, respectively. (E) Mineralogy of the Oroya alteration zone shown in a false-colored, SEM-BSE-EDS image with modal percentages given on the corresponding graph. Oroya alteration comprises sericite, albite, quartz, sulfide, ankerite, and Ti-V oxide. (F) Isocon diagram illustrating the elemental gains and losses associated with Oroya alteration. The isocon slope of ~ 1 is indicative of constant mass in the alteration zone. (G) Histogram diagram displaying the elemental changes recorded in Oroya alteration as percentage change. Gold grades in the least-altered sample and altered sample are 0.003 ppm and 6.11 ppm, respectively

moderately SW-dipping reverse shear band that offsets the mesocratic intrusion and the HS2 veins (Fig. 6C).

Other D_{2b} lode offset faults are visible in the 290 m RL south and 310 m RL north drives. In the 290 m RL south drive, a banded vein hosted in dark, least-altered Williamstown Dolerite is offset by a N-striking, steeply W-dipping D_{2b} normal fault and juxtaposed against Devon Consols Basalt (ESM Fig. 5A, B). In the 310 m RL north drive, a foliated, NW-striking, steeply SW-dipping banded vein hosted in carbonate-fuchsite-quartz–altered Williamstown Dolerite is offset in an apparent normal sense by a NNE-striking, steeply W-dipping D_{2b} fault (ESM Fig. 5C). In another area of the 310 m RL north drive, a banded and foliated vein in carbonate-fuchsite-quartz–altered Williamstown Dolerite is offset by an E-striking, steeply S-dipping D_{2b} fault with sub-horizontal slickenlines (ESM Fig. 5D). The banded vein, foliation, and fault are cross-cut by NE- to ENE-striking, moderately to steeply N-dipping D_3 stockwork veins (ESM Fig. 5E).

Along the 230–240 m RL incline, the D_{2c} Cadiz fault zone is exposed (Fig. 7A). The fault zone is ~ 2 m wide and offsets carbonate-fuchsite-quartz–altered Williamstown Dolerite in the footwall from dark, least-altered Williamstown Dolerite in the hanging wall (Fig. 7A). The fault zone contains NW- to NNW-striking, sub-vertical to moderately SW-dipping $S_{2c}S$ and $S_{2c}C$ fabrics defining a reverse sense of shear zone movement (Fig. 7B). Deformed laminated veins similar to the HS2 veins at the 290 m RL south drive are present within the fault zone (Fig. 7C). Tension gashes are spatially linked to D_{2c} fault-fill veins (Fig. 7D), and moderately SSW-plunging slickenlines are on $S_{2c}C$ surfaces (Fig. 7E); both of the aforementioned relate to D_{2c} reverse movement in the fault zone.

Deformed, banded D_{2b} Hidden Secret veins within dark, least-altered Williamstown Dolerite are exposed along the 430 m RL south drive (ESM Fig. 6). The banded veins are cross-cut by D_3 stockwork veins, which locally define asymmetric folds related to D_3 reverse movement (ESM Fig. 6). Reverse movement related to the D_3 stockwork veins is further emphasized by NW- to WNW-striking, steeply to moderately SW-dipping S_3C, S_3C', and S_3S fabric geometries (ESM Fig. 6). A SW-plunging slickenline is sub-parallel to the dip of the S_3C fabric, and the S_3S fabric is axial planar to the folded stockwork veins.

In nearby diamond drill hole TFUD0036 (Fig. 1A), a zoned hydrothermal alteration halo is developed around a leucocratic dike (Fig. 8A, B). The alteration zone transitions symmetrically from dark, least-altered Williamstown Dolerite (Fig. 8C), to tan, quartz-carbonate-Cr-chlorite-altered dolerite (Fig. 8D), to green, carbonate-fuchsite-quartz–altered dolerite (Fig. 8E).Within the carbonate-fuchsite-quartz-altered, a NW-striking, sub-vertical S_2 cleavage is developed (Fig. 8F); fragments of the cleaved dolerite occur within the leucocratic dike (Fig. 8B).

Alteration mineralogy and mass balance calculations

Results of whole-rock geochemical analysis and mineralogy for the alteration mass balance are presented in ESM Appendix 2. The calculated elemental gains and losses relative to least-altered samples as well as the scaling factors used for the isocon diagrams are given in ESM Appendix 3.

Fimiston At location 2 in the Super Pit (Fig. 2A), proximal Fimiston alteration (Fig. 4A, B) shows extreme enrichments (> 250%; Fig. 4C, D) for Au, Te, W, S, and Hg. Strong enrichments (100–250%) are shown for Rb, K_2O, Cs, and As. In proximal Fimiston alteration from drill hole OLDG0001G (Fig. 1A), extreme enrichments are shown for Au, W, Te, As, S, Sb, and K_2O; strong enrichments are shown for Cs and Rb. When proximal Fimiston alteration from location 2 is compared to that from OLDG0001G, both samples show strong to extreme enrichment in Au, Te, W, S, Rb, K_2O, Cs, and As.

Oroya Proximal Oroya alteration (Fig. 4A, E) in Golden Mile Dolerite at location 2 in the Super Pit (Fig. 2A) shows extreme enrichments (Fig. 4F, G) for Au, Te, S, Hg, V, W, Ag, Tl, As, Rb, K_2O, and Cs. Barium shows a strong

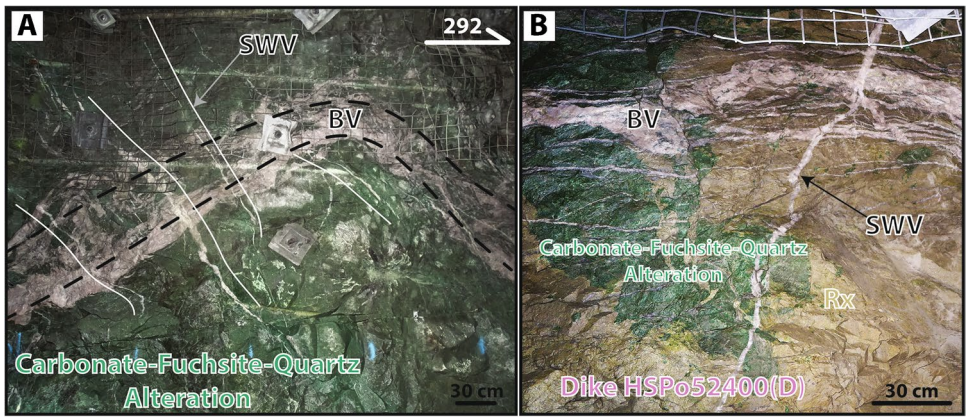

Fig. 5 Hidden Secret underground relationships (310 m RL south drive). **A** Folded banded vein (BV) surrounded by proximal, carbonate-fuchsite-quartz alteration (looking SSW in a vertical face). The banded vein is cross-cut by late stockwork veins (SWV). **B** Carbonate-fuchsite-quartz alteration is intruded by a leucocratic dike (HsPo 52400(D)); wall rock assimilation is indicated by tan-colored reaction zones (Rx). The carbonate-fuchsite-quartz alteration and dike are cross-cut by a banded vein (BV), which is in turn cross-cut by a late stockwork vein (SWV)

enrichment. When compared to the samples of Fimiston alteration (ESM Fig. 7A, B), Oroya alteration shows similar Au, Te, S, W, As, Rb, K_2O, Cs, and Ba enrichments, but the Au, Te, Hg, and S enrichments are much higher in Oroya alteration. Furthermore, Oroya alteration is characterized by extreme V, Ag, and Tl enrichments that are not defined in the Fimiston alteration samples.

Hidden Secret Mass balance calculations of the distal alteration (Fig. 8A, D) record extreme enrichment in (Fig. 9A) Cu, S, W, Te, Bi, Au, As, and Sb. Mass balance calculations of the proximal alteration (Fig. 8A, E) record extreme enrichment (Fig. 9B) in Te, As, K_2O, S, Rb, Ba, Au, Cu, and Sb. When the mass balance calculations of the distal and proximal alteration are compared, both show similar enrichments in Te, As, S, Au, Cu, Sb, and C, but the proximal alteration shows a higher level of enrichment in Au, As, and Te. Furthermore, the proximal alteration shows extreme K_2O, Rb, and Ba enrichment that is not present in the distal alteration. When the proximal Hidden Secret alteration is compared to the proximal Fimiston alteration, both alteration types show Au-Te-As-S-K_2O-Rb-C-Ba enrichment. Fimiston alteration lacks the Cu enrichment in proximal and distal Hidden Secret alteration and also the Bi enrichment of the distal Hidden Secret alteration. Like the proximal Fimiston alteration, the proximal Hidden Secret alteration lacks the extreme V, Ag, and Tl enrichments observed in proximal Oroya alteration and the Au, Te, Hg, and S enrichments are lower than they are for proximal Oroya alteration (ESM Fig. 7A, B).

LA-ICP-MS pyrite analysis

The results of LA-ICP-MS pyrite analysis are given in ESM Appendix 4. Fimiston pyrite shows strong (≥ 0.6, $p < 0.05$) Au-Ag, Au-Te, and Au-Tl correlations (ESM Fig. 7C, D, E). Hidden Secret pyrite also shows strong Au–Ag and Au-Te correlations (ESM Fig. 7C, D, E). Oroya pyrite shows strong Au–Ag and Au-Te correlations as well as strong Au-Cu, Au-As (ESM Fig. 7G), Au–Ag, Au-Sb, Au-W, Au-Tl, Au-Pb, Au-Ga, Au-V, and Au-Bi correlations (ESM Fig. 7C, D, E). When the different pyrite types are compared, Fimiston, Hidden Secret, and Oroya pyrite all show strong Au-Ag and Au-Te correlations. Fimiston pyrite is distinguished from Hidden Secret pyrite by a strong Au-Tl correlation. Oroya pyrite is distinguished from Fimiston and Hidden Secret pyrite by strong Au-Cu, Au-As, Au–Ag, Au-Sb, Au-W, Au-Pb, Au-V, Au-Ga, and Au-Bi correlations.

Box plots emphasize significant overlap in the absolute concentrations of Ag, As, Cu, Pb, Sb, Te, V, and Zn in Fimiston, Oroya, and Hidden Secret pyrite (ESM Fig. 7H). Fimiston and Oroya pyrites contain similar median Au values (2.88 and 2.70 ppm, respectively), which are higher than the value in Hidden Secret pyrite (0.20 ppm). Hidden Secret pyrite shows a marked Bi enrichment (2.67 ppm median) when compared to Fimiston and Oroya pyrite (0.15 and 0.01 ppm, respectively). Fimiston pyrite is enriched in Tl (0.38 ppm median) relative to Oroya and Hidden Secret pyrites (0.10 and 0.02 ppm, respectively).

When the pyrite from the proximal Hidden Secret alteration is compared to pyrite from the Hidden Secret HS1

and HS2 veins, Au-Te and Au–Ag correlations are very similar in the different populations (0.79–0.91; $p < 0.05$; ESM Fig. 7D, E). The Ag:Au ratios are higher in pyrite from the HS1 and HS2 veins than in the pyrite from the proximal alteration (ESM Fig. 7D). When absolute elemental values are considered (ESM Fig. 7I), the median value for Au is highest in the HS2 vein pyrite (2.06 ppm) and lower in both the HS1vein pyrite and proximal alteration pyrite (0.08 and 0.12 ppm, respectively). Median values for values for Ag, Cu, Pb, Sb, Te, Tl, V, and Zn show progressive enrichment from proximal alteration pyrite to HS1 vein pyrite to HS2 vein pyrite (ESM Fig. 7I). Median As values are similar for HS1 vein pyrite and HS2 vein pyrite (95.44 and 70.15 ppm, respectively); the median value for pyrite from proximal Hidden Secret alteration is significantly higher (2874.45 ppm).

Multiple sulfur isotope analysis

The results of multiple sulfur isotope analysis in pyrite from proximal Oroya alteration (Fig. 4E), Hidden Secret HS1 veins (Fig. 6A, B), and proximal Hidden Secret alteration (Fig. 8E, F) are given in Appendix 5. In Fig. 10A, B), the results are plotted with data from Godefroy-Rodríguez et al. (2020a) and McDivitt et al. (2021a). Pyrite from the HS1 veins ($n = 18$) ranges in $\delta^{34}S$ from − 10.75 to − 0.17‰. The $\Delta^{33}S_{pyrite}$ values in the HS1 veins define a restricted range from 0.06 to 0.19‰. Pyrite from proximal Hidden Secret alteration ($n = 11$) is restricted in range for both $\delta^{34}S$ and $\Delta^{33}S$. The $\delta^{34}S_{pyrite}$ values range from − 1.16 to 3.85‰, with 10 of the 11 values ranging from 3.42 to 3.85‰. The $\Delta^{33}S_{pyrite}$ values are higher than those in the HS1 veins and range from 0.25 to 0.43‰. Pyrite from the Oroya alteration zone ($n = 14$) shows highly variable $\delta^{34}S$ from - 11.56 to - 4.96‰ and consistent $\Delta^{33}S$ values that range from 0.08 to 0.17‰.

Mineralogy and whole-rock geochemistry of the Hidden Secret dikes

Dikes HsPo 52400(D) (Fig. 5B), HsPo 52350 (Fig. 6C), and HsPo 52690 (Fig. 8A, B) are similar in their mineralogy (ESM Fig. 8A, B) and comprise albite (37–42%), carbonate (38–40%), quartz (10–15%), sericite (0–10%), sulfides (1–2.5%), apatite (0.5–1%), barite (0–0.5%), and a TiO_2 mineral (0–0.5%). Whole-rock geochemical data for the dikes is presented in ESM Appendix 6. On the basis of Nb/Y vs. Zr/TiO2 ratios, dike HsPo 52690 is dacitic and dikes HsPo 52400(D) and HsPo 52350 are andesitic (ESM Fig. 8C) in composition.

Discussion

Constraints on the structural setting and relative timing of gold-telluride lode mineralization

The Fimiston and Hidden Secret lodes both preferentially strike NW and range from sub-vertical to moderately SW dipping (ESM Fig. 1A, C). Like the Fimiston lodes, the Hidden Secret lodes are deformed by a NNW-striking, sub-vertical cleavage (ESM Fig. 1B, D), folded (Figs. 6 and 9A), and cross-cut by late D_3 stockwork veins (Fig. 5A) that are similar in orientation to the stockwork veins in the Mt. Charlotte orebody (ESM Fig. 1E, F). Evidence for D_{2b} normal deformation associated with Fimiston lode development is present as upward-pointing acute vein bifurcations (ESM Fig. 2A), the normal drag of S_{2b} fabrics along lode margins (ESM Fig. 2D), and asymmetric breccia clasts that record a normal shear component (ESM Fig. 2C). In the Hidden Secret orebody, hessite-bearing HS1 veins are offset by a N-striking, sub-vertical D_{2b} fault which hosts hessite-bearing HS2 veins related to normal deformation (Fig. 6A–D). Pyrite from both the HS1 and HS2 veins shows similar Au–Ag and Au-Te correlations and elevated Ag:Au ratios in comparison to Fimiston and Oroya pyrites (ESM Fig. 7D, E). Therefore, it is likely that both the HS1 and HS2 veins record the same hydrothermal event and D_{2b} structural environment. Additional evidence for D_{2b} normal deformation in the Hidden Secret orebody is shown by similar N-striking lode offset faults (ESM Fig. 5A, B, C). Other E-striking lode offset faults are cross-cut by stockwork veins (ESM Fig. 5D, E), suggesting that the development of the lode offset faults predated the D_3 Mt. Charlotte stockwork vein event and likely reflect D_{2b} transtension.

Where the D_{2b} Fimiston lodes are cross-cut by low-angle D_{2c} Oroya mineralization (Fig. 4A); ESM Fig. 4A), the lodes are overprinted by reverse deformation as shown by reverse S_{2c}S-S_{2c}C fabrics developed along the lode margins (ESM Fig. 4D). Similar D_{2c} reverse deformation overprints the D_{2b} Hidden Secret lodes (Fig. 6C), and Hidden Secret lode mineralization is cross-cut by the D_{2c} Cadiz reverse fault zone (Fig. 7A), which is similar in its geometry and kinematics to the Oroya hanging wall and footwall D_{2c} thrusts in the Oroya shoot (Mueller 2020a). These relationships suggest that, like the Fimiston lodes, the Hidden Secret lodes also pre-date the D_{2c} event and its associated Oroya style mineralization. Because both the Fimiston and Hidden Secret lodes pre-date D_{2c}, and there are D_{2b} extensional structures associated with both types of lode mineralization, it is probable that like the Fimiston lodes, the Hidden Secret lodes also developed during D_{2b} transtension, at a time when the Towns fault facilitated the development of a releasing bend (Fig. 11A, B).

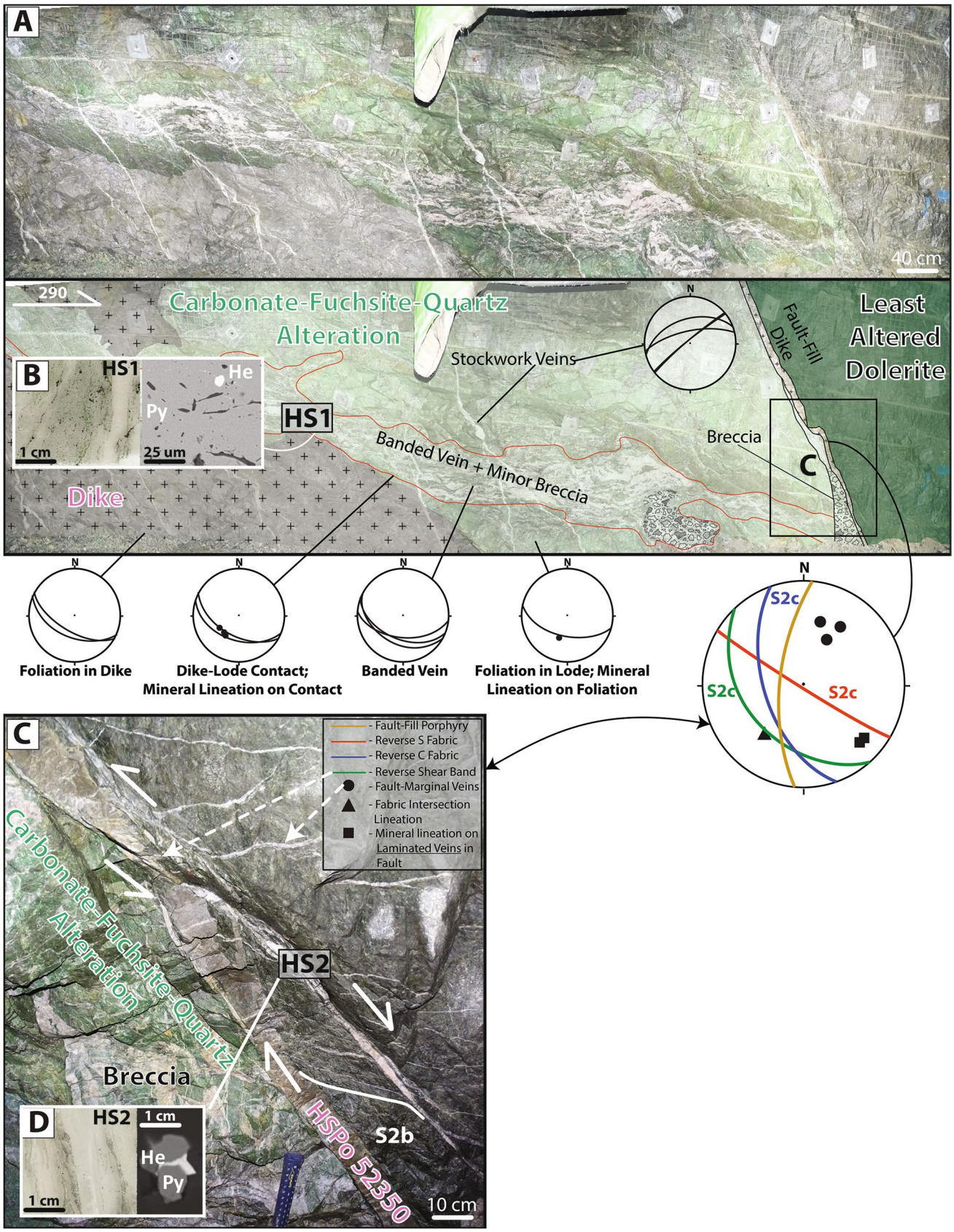
A
40 cm
290
Carbonate-Fuchsite-Quartz Alteration
Stockwork Veins
Fault-Fill Dike
Least Altered Dolerite
B
HS1
He
Py
1 cm
25 um
HS1
Banded Vein + Minor Breccia
Breccia
C
Dike
N
Foliation in Dike
Dike-Lode Contact; Mineral Lineation on Contact
Banded Vein
Foliation in Lode; Mineral Lineation on Foliation
S2c
S2c
S2c
C
- Fault-Fill Porphyry
- Reverse S Fabric
- Reverse C Fabric
- Reverse Shear Band
- Fault-Marginal Veins
- Fabric Intersection Lineation
- Mineral lineation on Laminated Veins in Fault
Carbonate-Fuchsite-Quartz Alteration
HS2
Breccia
D
HS2
1 cm
He
Py
1 cm
HSPO 52350
S2b
10 cm

◂**Fig. 6** Hidden Secret underground relationships (290 m RL south drive). (A) Sub-vertical exposure (looking SSW) of a lode comprising a WNW- to W-striking, moderately S-dipping banded and brecciated HS1 vein in carbonate-fuchsite-quartz alteration. A leucocratic dike occurs in the hanging wall and footwall to the lode. A WNW-striking, moderately to steeply south dipping cleavage is developed within the lode and the intrusion, and a mineral lineation plunges moderately to steeply SW along the intrusion-lode contact and along the cleavage. Late stockwork veins that are WSW- to SW-striking and sub-vertical to moderately N-dipping cross-cut the deformed lode. On the right side of the image, the lode and carbonate-fuchsite-quartz alteration are offset by a N-striking, steeply W-dipping fault filled with a mesocratic dike and juxtaposed against least-altered (dark) Williamstown Dolerite. (B) Scanned thin section (left) and SEM-BSE image (right) of the banded HS1 Hidden Secret lode vein. The SEM-BSE image displays hessite (He) as a bright inclusion within pyrite (Py). (C) Close-up of the mesocratic fault-fill dike shown in (A). The fault-fill dike (HsPo 52350) is offset by a NW-striking, moderately SW-dipping S_{2c} reverse shear band that is associated with a NW-striking, sub-vertical $S_{2c}S$ fabric and a NNW-striking, moderately W-dipping $S_{2c}C$ fabric. In the hanging wall of the fault, NW-striking, moderately SW-dipping marginal veins are developed and linked with laminated HS2 veins that parallel the fault zone. The marginal veins are dragged along the dike and HS2 veins with S_{2b} fabrics defining a normal sense of shear movement. (D) Scanned thin section (left) and SEM-BSE image (right) of the laminated HS2 vein. The SEM-BSE image displays hessite (He) intergrown with pyrite (Py)

Further evidence that the Fimiston and Hidden Secret lodes were formed as part of a single mineralization event is provided by alteration mass balance, the LA-ICP-MS pyrite dataset, and by dikes in the Hidden Secret orebody. Both the Fimiston and Hidden Secret alteration show similar Au-Te-As-S-K_2O-Rb-C-Ba enrichment in proximal alteration zones (Figs. 4D and 9B), lack the extreme levels of S, V, Hg, Te, and S enrichment shown in Oroya style alteration (ESM Fig. 7A, B), and show lower levels of Au and Ag enrichment than Oroya style hydrothermal alteration. Similarly, both the Fimiston and Hidden Secret pyrites show strong Au-Ag and Au-Te correlations, but lack the strong Au-Cu, Au-As, Au–Ag, Au-Sb, Au-W, Au-Pb, Au-V, Au-Ga, and Au-Bi correlations observed for pyrites from Oroya style mineralization (ESM Fig. 7C). Fimiston lode development occurred synchronously with the emplacement of mesocratic, hornblende-phyric porphyry dikes (Gauthier et al. 2004). The albite-carbonate-quartz dikes in the Hidden Secret orebody are mineralogically and geochemically similar to the syn-Fimiston hornblende-phyric porphyry dikes, with andesitic to dacitic compositions (ESM Fig. 8A, B; Woods 1997; McDivitt et al. 2020). The dikes intrude gold-bearing Hidden Secret proximal alteration (Figs. 5B and 8B), and cross-cut HS1 veins in the Hidden Secret orebody (Fig. 6A), and are deformed by D_{2C} deformation (Fig. 6C). Collectively, these relationships further indicate that the albite-carbonate-quartz dikes in the Hidden Secret orebody are syn-ore dikes and similar to the syn-ore dikes related to Fimiston mineralization. Radiometric ages reported for the Hidden Secret andesitic dikes in McDivitt et al. (in press) of (U–Pb SHRIMP zircon; 2σ) 2678 ± 4 Ma, 2672 ± 9 Ma, 2676 ± 6 Ma, 2678 ± 4 Ma, and 2680 ± 7 Ma are similar to other U–Pb SHRIMP zircon ages (2σ) reported for the hornblende-phyric porphyry dikes of 2667 ± 11 Ma and 2675 ± 3 Ma (data from Vielreicher et al. 2010 recalculated by McDivitt et al. 2020). These ages constrain the timing of both D_{2b} deformation and Fimiston/Hidden Secret mineralization to ca. 2675 Ma (Fig. 11A).

Foliation development and gold-telluride lode deformation

Because the D_{2b} Fimiston lodes are deformed by a NNW-striking, sub-vertical cleavage and the D_3 Mt. Charlotte stockwork veins cross-cut the cleavage, the cleavage is considered to be a key structural marker in the chronological development of the district (Gauthier et al. 2004; Tripp 2013). The formation of this cleavage is typically attributed to the ENE-WSW shortening conditions of D_2 and either associated with compression (Weinberg et al. 2005; Tripp 2013) or sinistral transcurrent shear zone movement (Swager 1989). The cleavage is interpreted to have formed during a single episode of late-stage deformation and metamorphism from ca. 2650 to 2640 Ma (Tripp 2013). McDivitt et al. (2021a) constrain the development of a NNW-striking, sub-vertical S_{2a} cleavage to 2680 ± 3 Ma. In this study, there is evidence for NNW-striking, sub-vertical cleavage development during ca. 2675 Ma D_{2b} when the cleavage was dragged along Fimiston lodes in a normal sense and cross-cut by the lodes (ESM Fig. 2D, F). There is also evidence for NNW-striking, sub-vertical cleavage development during D_{2c} when the lodes were drag folded and deformed during reverse movement (ESM Figs. 3 and 4). There is further evidence for NNW-striking, sub-vertical cleavage development during D_3 stockwork vein emplacement in the Hidden Secret orebody (ESM Fig. 6), when early D_{2b} lode structures were subjected to a D_3 reverse reactivation. Because D_2 structures, such as the D_{2b} Fimiston lodes and D_{2c} Oroya thrust faults, are similar in strike to the NNW-striking, sub-vertical cleavage, it is likely that the S_{2b} and S_{2c} cleavages record preferred flattening during the ENE-WSW regional bulk shortening of D_2. In contrast, because major D_3 faults are N- to NE-striking and have dextral kinematics, it is likely that D_3 bulk shortening differed from D_2. Hence, the similar NNW-striking, sub-vertical S_3 cleavage geometry in the Hidden Secret orebody (ESM Fig. 6) may record the influence of an anisotropy inherited from earlier lodes on cleavage development during D_3 (cf. Treagus 1983). Importantly, these results illustrate that the development of a NNW-striking, sub-vertical cleavage in the Golden Mile occurred over a protracted history during both D_2 and D_3 deformation events (Fig. 11A) rather than during a single late-stage event as suggested by Tripp (2013). Furthermore,

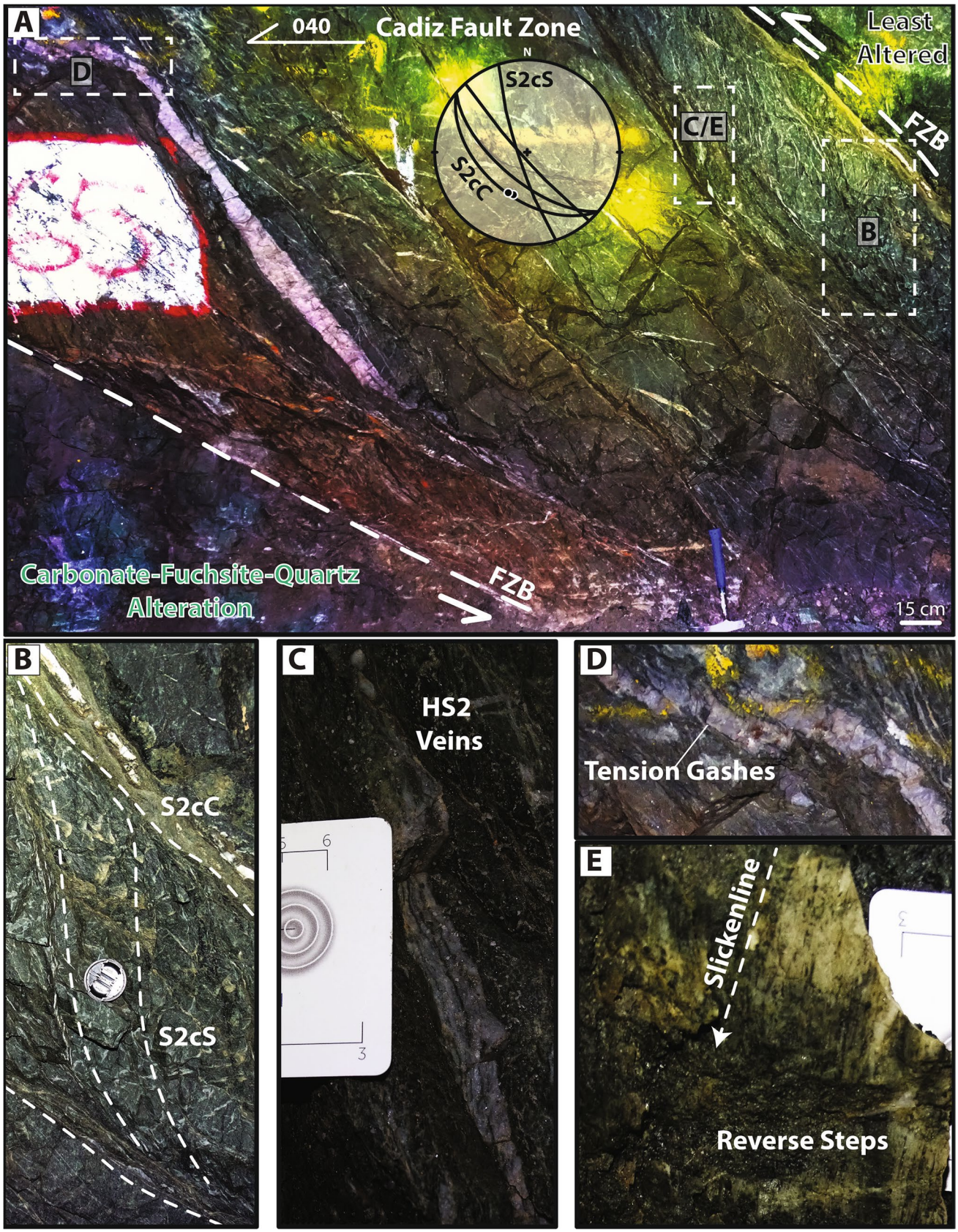
A
040
Cadiz Fault Zone
N
S2cS
S2cC
D
C/E
B
Least
Altered
FZB
Carbonate-Fuchsite-Quartz
Alteration
FZB
15 cm
B
S2cC
S2cS
C
HS2
Veins
D
Tension Gashes
E
Slickenline
Reverse Steps

◂**Fig. 7** Hidden Secret underground relationships (230–240 m RL incline looking SE). (A) Carbonate-fuchsite-quartz–altered Williamstown Dolerite (lower left) juxtaposed against dark, least-altered Williamstown Dolerite (upper right) by the Cadiz fault zone; fault zone boundaries (FZB) are shown as the dashed, white lines. The stereonet depicts NW- to NNW-striking, sub-vertical $S_{2c}S$ fabric measurements and NW-striking, moderately SW-dipping $S_{2c}C$ fabric measurements along with a moderately SSW-plunging slickenline developed on the $S_{2c}C$ fabric. Low-angle tension gashes (upper left) linked to a fault-fill vein indicate reverse movement. (B) Close-up of the area indicated in (A) showing S-C fabric geometries defining a reverse sense of shear zone movement. (C) Close-up of the area indicated in (A) where deformed veins similar to the HS2 veins shown in Fig. 6 are present. (D) Close-up of the area indicated in (A) depicting low-angle tension gashes. (E) Close-up of the area indicated in (A) showing a slickenline developed on a C surface and steps indicating a reverse shear sense

since the NNW-striking, sub-vertical cleavage developed pre-, syn-, and post-Fimiston lode formation, the lodes do not entirely pre-date the formation of the cleavage as suggested by Gauthier et al. (2004). Accordingly, the cleavage should not be considered as a robust chronological marker in the evolution of the district.

Structural, geochemical, and magmatic evolution of the Hidden Secret orebody

Fluid inclusion (Parker 2016) and mass balance calculations suggest that the development of proximal Hidden Secret alteration records the ingress of an H_2O-CO_2 fluid enriched in Au, Te, As, Cu, Sb, and large-ion lithophile elements (LILE; Fig. 11B). The distal Hidden Secret alteration is a LILE-poor expression of this fluid's alteration (Fig. 11B). Because the Au-Te-Ag correlations in the LA-ICP-MS pyrite dataset are similar for the proximal Hidden Secret alteration, HS1 veins, and HS2 veins (ESM Fig. 7D-E), it suggests that the proximal Hidden Secret alteration, HS1 veins, and HS2 veins all record the same H_2O-CO_2 hydrothermal fluid system. The syn-ore dikes that intrude the proximal Hidden Secret alteration are cross-cut by HS1 veins (e.g., Fig. 5B), indicating that the proximal Hidden Secret alteration formed during an early stage of D_{2b} hydrothermal activity along the Towns fault when pervasive fluid flow (cf., Valley 1986) was favored. Progressive D_{2b} deformation along the Towns fault lead to the development of a releasing bend (Fig. 11B), which was associated with low mean stress and increased fracture density resulting in a suction pump effect on hydrothermal fluids (Sibson 1987, 2001; Cox 2005), and the formation of HS1 veins and HS2 veins in a D_{2b} transtensional setting where channelized fluid flow (e.g., Valley 1986) was dominant. During later D_{2c} deformation, the Cadiz and Salamanca faults offset and deformed the proximal Hidden Secret alteration, HS1 veins, and HS2 veins during the development of the S_{2c} cleavage (Fig. 7A, B). During D_3, stockwork veins cross-cut the HS1 veins (Figs. 5A and 6A), and the lode structures were subjected to a reverse reactivation during the development of the S_3 cleavage (ESM Fig. 6). It was likely during these later D_{2c} and D_3 events that the Hidden Secret lodes were folded (e.g., Fig. 5A) and the moderate SE ore plunge was established (Fig. 5B), as the ore plunge orientation is similar to that of S-C fabric intersections in the D_{2c} Cadiz fault zone (Fig. 7A) and also to S_3C-S_3S intersections in zones of D_3 deformation (ESM Fig. 6).

Geochemical differences are evident when assessing the different paragenetic stages of the Hidden Secret orebody (i.e., proximal Hidden Secret alteration, HS1 veins, HS2 veins). The $\delta^{34}S_{pyrite}$ values in proximal Hidden Secret alteration are more positive and restricted in their distribution than the variably negative HS1 vein $\delta^{34}S_{pyrite}$ values (Fig. 10B). Because Au-Ag-Te systematics in the LA-ICP-MS pyrite dataset are similar for both proximal Hidden Secret alteration and the HS1 vein pyrite (ESM Fig. 7D, E), it is not likely that the differences in the $\delta^{34}S_{pyrite}$ values are attributable to different hydrothermal fluid systems. As $\delta^{34}S_{pyrite}$ is sensitive to intensive fluid conditions (e.g., fO_2, pH), it is possible that changes in physico-chemical fluid parameters such as fO_2 may explain the differences between the proximal Hidden Secret alteration and HS1 vein $\delta^{34}S_{pyrite}$ values (e.g., Phillips et al. 1986; Evans et al. 2006; Hodkiewicz et al. 2009; Godefroy-Rodríguez et al., 2020a). In consideration of $\Delta^{33}S_{pyrite}$, the values in the HS1 veins are consistently lower than those from the proximal Hidden Secret alteration (Fig. 10B). This suggests that the different $\delta^{34}S_{pyrite}$ values in the proximal Hidden Secret alteration and HS1 veins correlate with different sulfur reservoirs: one which contains a MIF signature ($\Delta^{33}S = 0.25$ to 0.43‰) greater than the traditionally proposed MIF limit ($\Delta^{33}S \sim 0.2$‰; Farquhar and Wing 2003) and one that does not ($\Delta^{33}S = 0.06$ to 0.19‰). Because pyrite within the proximal Hidden Secret alteration records conditions of pervasive fluid flow during the development of the alteration, it records an environment of relatively low fluid:rock ratio and it is likely that interaction with the Williamstown Dolerite or perhaps the nearby Kapai Slate country rock contributed local MIF sulfur ($\Delta^{33}S = 0.25$ to 0.43‰) to the fluid. Pyrite within the HS1 veins records channelized fluid flow conditions during vein formation within a releasing bend (Fig. 11B) and an environment of relatively high fluid:rock ratio. Hence, the lower $\Delta^{33}S_{pyrite}$ values in the HS1 vein likely approximate the original fluid values ($\Delta^{33}S = 0.06$ to 0.19‰). In this case, the negative $\delta^{34}S$ values in the HS1 veins are not explained by oxidation due to local fluid-rock interaction (e.g., Philips et al. 1986; Evans et al. 2006). In contrast, the effects of fluid-rock interaction during the development of the proximal Hidden Secret alteration under a pervasive flow regime yielded a restricted $\delta^{34}S_{pyrite}$ range of 3.42 to 3.85‰ that is consistent with decreased fluid fO_2 under greenstone-buffered

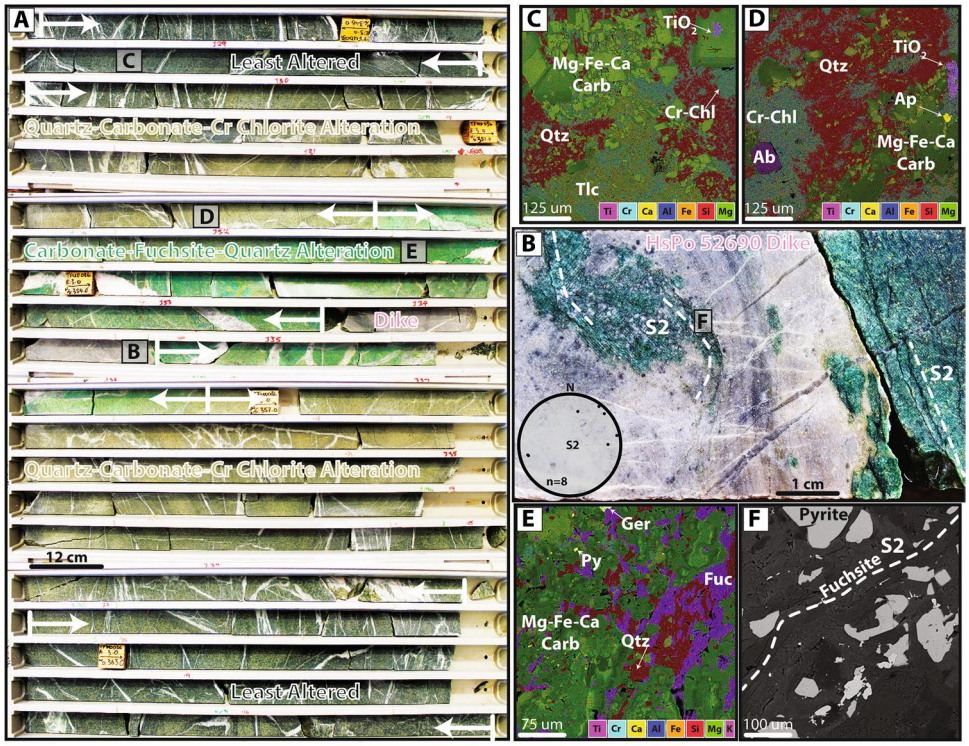

Fig. 8 Hidden Secret drill core relationships (TFUD0036 347–366 m). (A) Symmetrically zoned alteration surrounding a leucocratic dike in altered Williamstown Dolerite. (B) Close-up of the dike shown in (A) where it is in contact with proximal carbonate-fuchsite-quartz alteration. An S_2 foliation is developed in the carbonate-fuchsite-quartz alteration, and S_2-foliated fragments are entrained as xenoliths in the intrusion. The intrusion and the S_2 foliation are cross-cut by late-stage tension gashes. Stereonet (lower hemisphere, equal area) displays S_2 foliation measurements from the drill hole. (C) Mineralogy of least-altered Williamstown Dolerite shown in a false-colored SEM-BSE-EDS image: Mg-Fe-Ca carbonate (carb), quartz(Qtz), Cr-chlorite (Chl), talc (Tlc), and TiO_2 mineral. (D) Mineralogy of distal quartz-carbonate-Cr-chlorite alteration shown in a false-colored SEM-BSE-EDS image: quartz (Qtz), Mg-Fe-Ca carbonate (carb), Cr-chlorite (Chl), albite (Ab), and apatite (Ap). (E) Mineralogy of proximal carbonate-fuchsite-quartz alteration shown in a false-colored SEM-BSE-EDS image: Mg-Fe-Ca carbonate (carb), fuchsite (Fuc), quartz (Qtz), pyrite (Py), and gersdorffite (Ger). (F) Close-up of the area indicated in (B). An SEM-BSE image displays the S_2 foliation defined by preferentially oriented fuchsite grains

conditions (Fig. 12). Overall, the sulfur isotope data from the Hidden Secret orebody supports a model whereby an oxidized, magmatic-hydrothermal ore-forming fluid with mantle-like $\Delta^{33}S$ (e.g., Mueller et al., 2020a) was locally reduced during fluid-rock interaction in alteration zones.

The progressive Ag, Cu, Pb, Sb, Te, Tl, V, and Zn enrichment in LA-ICP-MS pyrite data from Hidden Secret proximal alteration to the HS1 and HS2 veins (ESM Fig. 7I) suggests that fluid fO_2 imparted a strong control on pyrite geochemistry (Xing et al. 2019; Godefroy-Rodríguez et al., 2020b). During early pervasive fluid flow, when the proximal Hidden Secret alteration developed, the decreased concentrations of these metals in pyrite may reflect the diminished solubility of these metals due to lowered fO_2 conditions resulting from buffering by the ferrous Williamstown Dolerite (Fig. 12). In contrast, the HS1 and HS2 veins developed in channelized flow regimes where fluid-rock interaction with the Williamstown Dolerite was diminished, suggesting that the increased Au, Cu, Pb, Sb, Te, Tl, V, and Zn concentrations in HS1 and HS2 pyrite may reflect the increased solubility of these metals under high fO_2 conditions (Fig. 12). Hidden Secret mineralization is distinguished from Fimiston mineralization by Bi and Cu enrichments in proximal and distal alteration, respective Au depletion and Bi enrichment in LA-ICP-MS pyrite data, and higher Ag:Au ratios in LA-ICP-MS pyrite data. As suggested by Mueller and Muhling (2013), these distinctions likely reflect the formation of the Hidden Secret lodes in the distal portion of a laterally zoned, camp-scale hydrothermal system.

Constraints on the nature of Oroya mineralization

It is well-documented that Oroya mineralization is characterized by a distinct V enrichment (Tomich 1958; Nickel 1977; Mueller 2020b; Mueller and Muhling 2020; Mueller et al. 2020a). However, most of the well-characterized samples come from the Oroya shoot area (Fig. 2A) in proximity to the Golden Mile Dolerite-Paringa Basalt contact at

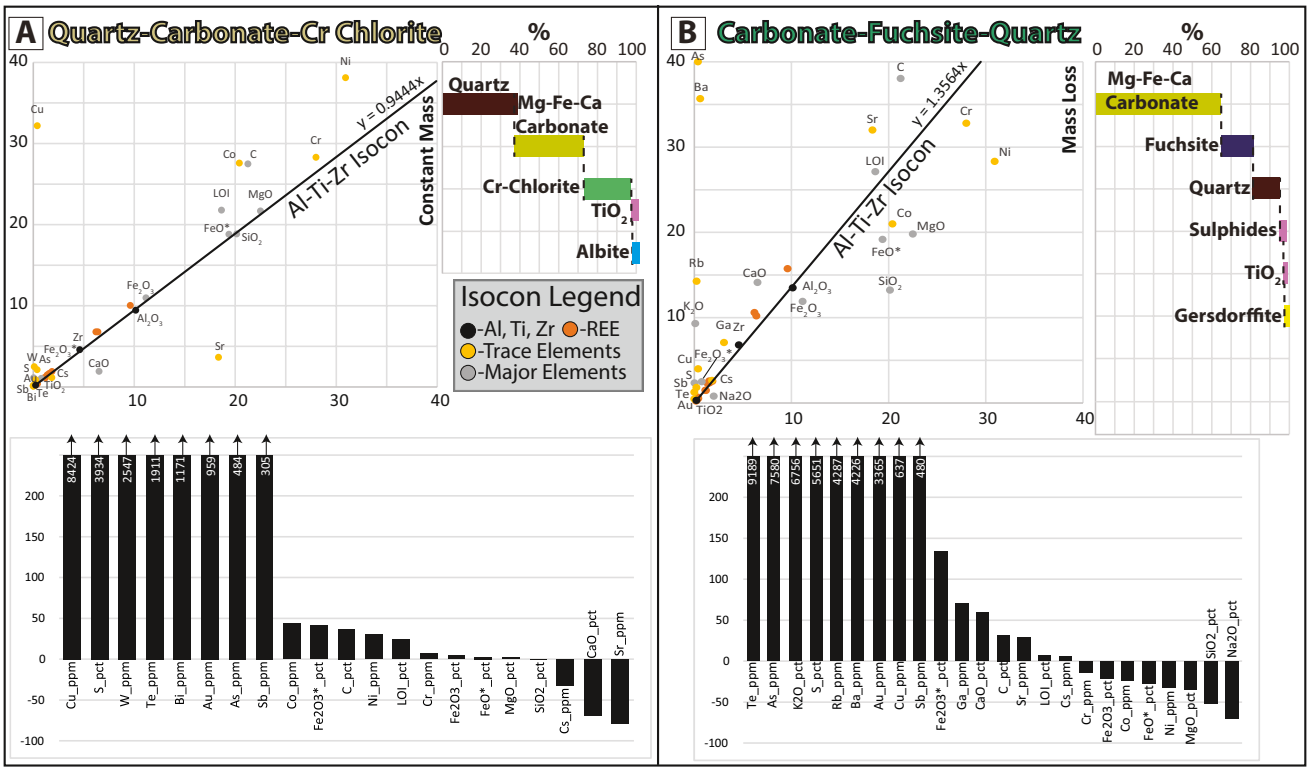

Fig. 9 Hidden Secret mass balance for distal quartz-carbonate-Cr-chlorite alteration (**A**) and proximal carbonate-fuchsite-quartz alteration (**B**). Isocon diagrams use scaled values (Grant 1986). Whole-rock geochemistry is given in ESM Appendix 2 and relative elemental changes are given in ESM Appendix 3. Isocon diagrams display the elemental gains and losses associated with alteration and the histogram diagrams display the elemental changes as percentage change. The isocon slope of ~ 1 is indicative of constant mass in the distal quartz-carbonate-Cr-chlorite alteration zone. The isocon slope of > 1 is indicative of constant mass in the proximal carbonate-fuchsite-quartz alteration zone. Modal mineralogy of the alteration types is displayed in the upper right portions of the figures. Gold grades in the least-altered sample, distal quartz-carbonate-Cr-chlorite alteration, and proximal carbonate-fuchsite-quartz alteration are 0.002 ppm, 0.020 ppm, and 0.094 ppm, respectively

the Oroya Shale horizon (e.g., Godefroy-Rodríguez et al., 2020a; Mueller 2020b; Mueller and Muhling 2020; Mueller et al. 2020a). Pronounced MIF $\Delta^{33}S_{pyrite}$ anomalies in Oroya shoot mineralization (Fig. 10A, B) are typically attributed to interaction with local sedimentary wall rock such as the Oroya Shale, where fluids were reduced to the pyrite-pyrrhotite stability field (Godefroy-Rodríguez et al., 2020a; Mueller et al. 2020a). As shale units may be enriched in V, As, Mo, Se, Ni, Ag, and Zn (VAMSNAZ suite; Large et al. 2011), it is possible that the distinct V enrichment in Oroya shoot mineralization records local interaction with the Oroya Shale or perhaps a shale-derived fluid source (Large et al. 2011). The sample of Oroya mineralization from location 2 (Fig. 2A) is distal from the Oroya Shale horizon. The $\Delta^{33}S_{pyrite}$ values (0.08 to 0.17‰) do not record an interaction with the Oroya Shale, suggesting that the well-defined V enrichment in mass balance calculations (Fig. 4G) and the Ti-V oxides in the alteration assemblage record a V component of Oroya hydrothermal fluid that was not sourced from local shale units (Fig. 4E). The Oroya pyrite analyzed at location 2 in the Golden Mile Dolerite did not return the same positive $\delta^{34}S_{pyrite}$ and MIF $\Delta^{33}S_{pyrite}$ values as documented by Godefroy-Rodríguez et al. (2020a) for Oroya mineralization in the Oroya shoot area (Fig. 10B). Because the Oroya sample from location 2 is distal from the Oroya shoot area, it supports the conclusions of Mueller et al. (2020a) that the $\delta^{34}S_{pyrite}$ and $\Delta^{33}S_{pyrite}$ values in Oroya Stage 1 and Stage 2 reflect the interaction of an oxidized magmatic fluid with the Oroya Shale (Figs. 10B; 12).

Implications for the formation and geochemistry of orogenic gold deposits

Singular vs. multiple mineralization events and genetic mechanisms Part of the argument used to support late-stage, broadly synchronous mineralization at ca. 2.64 Ga is the lack of a coherent structural framework to mineralization (Vielreicher et al. 2015b). The incorporation of the Hidden Secret mineralization type into the structural framework of the camp emphasizes a coherent and consistent structural framework that may be used to chronologically group gold mineralization styles (Fig. 11A). The

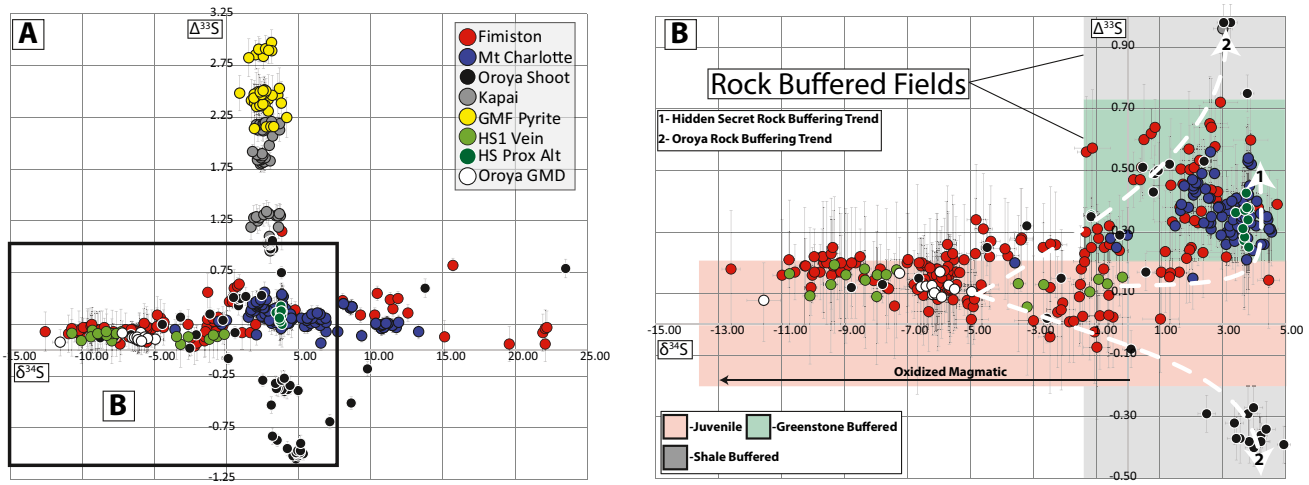

Fig. 10 Multiple sulfur isotope data from Hidden Secret and Oroya mineralization (ESM Appendix 5) integrated with data from Godefroy-Rodríguez et al. (2020a) and McDivitt et al. (2021a). (A) Compilation of multiple sulfur isotope data from different ore styles including Fimiston, Mt. Charlotte, Oroya shoot, Hidden Secret HS1 vein, Hidden Secret carbonate-fuchsite-quartz alteration (HS Prox Alt), and Oroya in the Golden Mile Dolerite (GMD) from location 2 in Fig. 2A. The Golden Mile fault (GMF) samples from McDivitt et al. (2021a) represent Fimiston and Oroya mineralization hosted in Lower Black Flag Group sedimentary rocks of the GMF. (B) Close-up of the area indicated in (A). The thick, dashed lines correspond to empirical trends that are inferred trends from inherently oxidized magmatic fluids in channelized flow regimes to greenstone belt rock-buffered fluids (1) and shale-buffered fluids (2) in pervasive flow regimes. Fluid interaction with local greenstone and shale wall rocks is interpreted to result in the restricted $\delta^{34}S$ ranges and non-zero $\Delta^{33}S$ ranges that characterize the rock-buffered fields

structural-hydrothermal framework outlined by this study (Fig. 11A) supports a model for punctuated mineralization from ca. 2.67 to 2.64 Ga (Bateman and Hageman 2004; Gauthier et al. 2004; Robert et al. 2005; Mueller 2020a). The Fimiston/Hidden Secret lodes formed during ca. 2675 Ma D_{2b} transtension, the Oroya lodes during ca. 2660 Ma D_{2c} contraction, and the later Mt. Charlotte stockwork veins from ca. 2650 to 2640 Ma during D_3 dextral shearing. This punctuated timing model for mineralization is similar to those suggested for other gold deposits of the Yilgarn craton such as the nearby Kanowna Belle deposit (Sugiono et al. 2021) and those of the Agnew district (Thébaud et al. 2018). The results of this and other studies emphasize that genetic models for orogenic gold deposits that account for punctuated mineralization within prolonged orogeny (in this case ca. 40 Ma) are likely more realistic than those that do not. The growing recognition that numerous orogenic gold deposits record multiple mineralization events and punctuated hydrothermal histories gives credibility to mineralization models that invoke multiple genetic mechanisms (e.g., Bateman and Hagemann 2004; Lawrence et al., 2013; McDivitt et al., 2018; Thébaud et al., 2018; Kerr et al., 2018; Masurel et al., 2019). Although the results of this study support magmatic-hydrothermal models for Fimiston/Hidden Secret and Oroya mineralization (e.g., Clout 1989; Bateman and Hagemann 2004; Mueller 2007; Mueller and Muhling 2013; Mueller and Muhling 2020; Mueller et al. 2020a), the late Mt. Charlotte stockwork veins differ in their structural timing, texture, mineralogy, and geochemistry when compared to the Fimiston, Hidden Secret, and Oroya gold-telluride lode types (McDivitt et al. 2020), and better adhere to late-stage gold mineralization models that invoke metamorphic devolatilization (e.g., Phillips 1986; Phillips et al. 1987, 1996; Groves et al. 2016; Vielreicher et al. 2016). Hence, it is likely that multiple, genetically distinct mineralization varieties are recorded in the camp's punctuated hydrothermal history, with magmatic-hydrothermal mineralization varieties represented by the early gold-telluride lodes and late metamorphic-hydrothermal mineralization represented by the Mt. Charlotte stockwork veins.

Mass balance and LA-ICP-MS pyrite data Mass balance calculations are useful to differentiate between the Fimiston/Hidden Secret and Oroya gold-telluride mineralization events: Fimiston and Hidden Secret are grouped distinctly from Oroya using multiple parameters including Au, Ag, Hg, Te, Ag, S, V, and Te (ESM Fig. 7A, B), with Oroya showing higher levels of enrichments in these elements than Fimiston and Hidden Secret. These results illustrate that alteration mass balance studies are useful in fingerprinting fluid chemistry and discriminating among multiple mineralization events in orogenic gold settings. Correlation coefficients in LA-ICP-MS pyrite data reveal a distinct trace metal signature for Oroya (strong Au-Cu, Au-As, Au–Ag, Au-Sb, Au-W, Au-Pb, Au-V, Au-Ga, and Au-Bi correlations) that is not present in the Fimiston and Hidden Secret mineralization

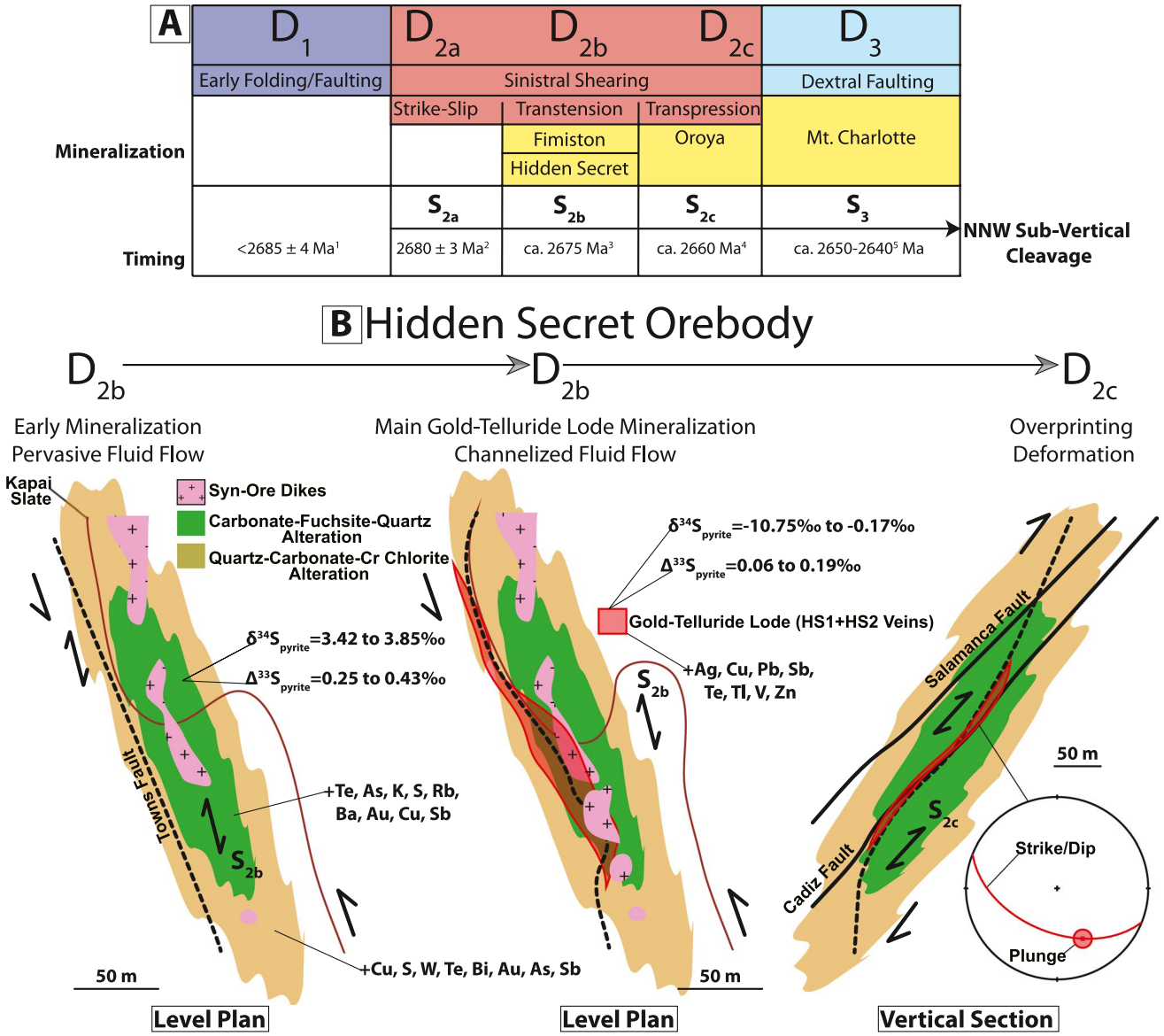

Fig. 11 **A** Chronological summary diagram for deformation and mineralization in the Kalgoorlie gold camp. *D_1 fold and thrust*: maximum age provided at 2685 ± 4 Ma by the Golden Mile Dolerite (Tripp 2013); minimum age provided at 2680 ± 3 Ma by a quartz-sericite-ankerite dike in the Golden Mile Fault zone (McDivitt et al. 2020). *D_{2a} sinistral strike-slip*: constrained at 2680 ± 3 Ma by a quartz-sericite-ankerite dike in the Golden Mile Fault zone (McDivitt et al. 2021a). *D_{2b} sinistral transtension*: interpreted at ca. 2675 Ma when pre-Fimiston quartz-feldspar porphyries and syn-Fimiston hornblende porphyries were emplaced (McDivitt et al. 2021a). Age constraints on the pre- and syn-Fimiston dikes are provided by Yeats et al. (1999), Gauthier et al. (2004), Vielreicher et al. (2010), and McDivitt et al. (2021a). *D_{2c} sinistral-reverse deformation*: represented by NW-striking thrust and reverse faults with sinistral strike-slip components that cross-cut and offset the D_{2b} Fimiston lodes and porphyries (i.e., Nepture, Flannagan, Cadiz, Salamance, Oroya thrusts). Inferred at ca. 2660 Ma based on the timing of similar structures in the Mt. Shea-Hannan's South area (Krapež et al. 2000; Fletcher et al. 2001; Mueller 2007). *D_3 dextral shearing*: represented by N- to NNE-trending dextral faults that are prominent in the Mt. Charlotte area. Constrained from ca. 2650 to 2640 Ma by the Liberty Granodiorite and U–Pb xenotime geochronology from Mt. Charlotte veins (Rasmussen et al. 2009; Vielreicher et al. 2010; Mueller et al. 2020b). **B** Schematic summary diagram illustrating the development of early mineralization and dikes during a D_{2b} pervasive fluid flow regime, and the formation of HS1 and HS2 main gold-telluride lode veins during a channelized fluid flow regime related to D_{2b} transtension. Overprinting deformation occurred during D_{2c} when the Cadiz and Salamanca faults cross-cut the gold-telluride lode mineralization

styles (ESM Fig. 7C). When the absolute concentrations of trace elements in pyrite are considered, there is significant overlap among the Fimiston, Hidden Secret, and Oroya mineralization styles (ESM Fig. 7H), emphasizing the conclusion of Godefroy-Rodríguez et al. (2020b) that absolute concentrations of trace elements in pyrite are not well-suited

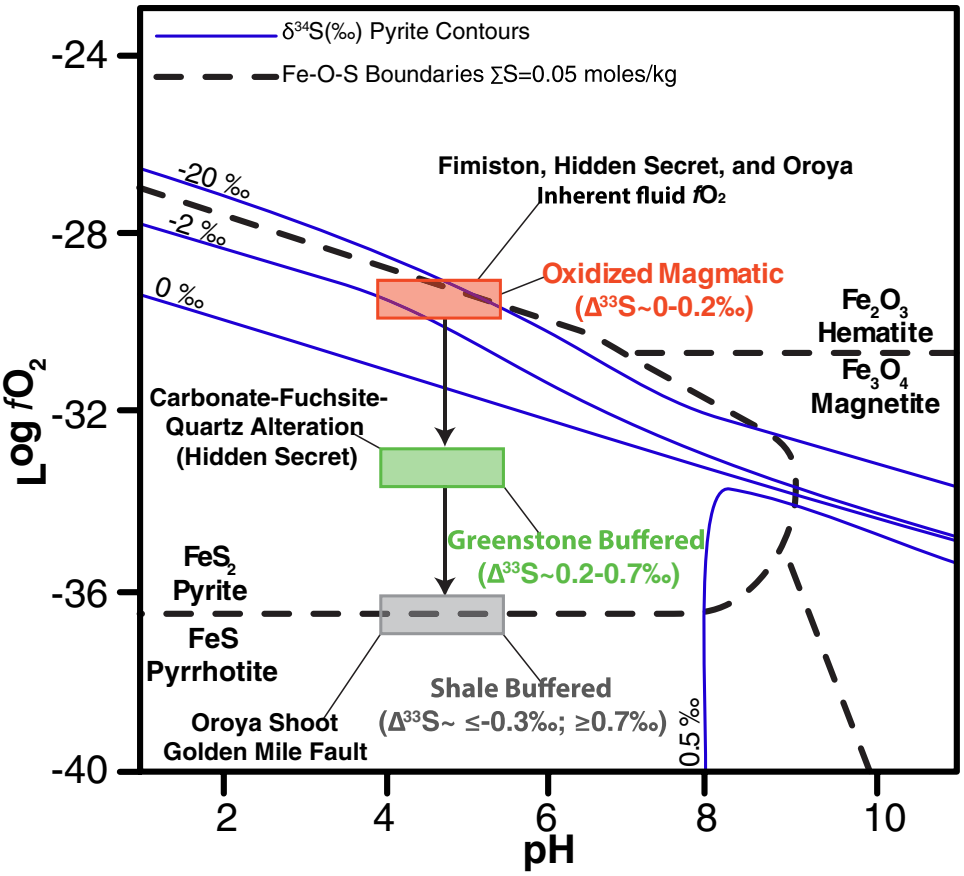

Fig. 12 The pH vs. fO_2 diagram adapted from Godefroy-Rodríguez et al. (2020a) and references therein. Experimental conditions are T = 300 °C, mNa+ = 1, mK+ = 0.1, mCa2+ = 0.01, and $\sum\delta^{34}S = 0‰$. Mineral stability fields in the Fe–O-S system ($\sum S = 0.05$ mol/kg) are shown as dashed lines. Blue lines are $\delta^{34}S$ values for pyrite and H_2S. Fimiston, Hidden Secret, and Oroya inherent fluid fO_2 conditions are represented by the red rectangle. Greenstone belt rock-buffered fO_2 conditions and shale-buffered fO_2 conditions are represented by the green and gray rectangles, respectively. The inferred fluid pH (4–5.5) is from Mueller et al. (2020a)

for discriminating different mineralization events. A good example of this is noted on the Au vs. V bivariate plot in ESM Fig. 7F, which shows that although Oroya pyrite has a distinct Au-V correlation relative to Fimiston and Hidden Secret pyrite (ESM Fig. 7C), the absolute concentration data from the different pyrite types overlaps significantly. These results and those of Godefroy-Rodríguez et al. (2020b) emphasize cautionary aspects in the use of absolute trace element concentrations in LA-ICP-MS pyrite datasets to discriminate and characterize the trace element signatures of different gold events. For these latter purposes, correlation coefficients derived from $\log_{10}$ LA-ICP-MS pyrite trace element data show better suitability, as shown by this study and that of McDivitt et al. (2021b).

Multiple sulfur isotopes Neither $\delta^{34}S_{pyrite}$ nor $\Delta^{33}S_{pyrite}$ shows good suitability in discriminating the Fimiston/Hidden Secret gold-telluride event from the Oroya gold-telluride event as the data show significant overlap (Fig. 10B). Hence, caution is emphasized in using these parameters in isolation to define and discriminate different gold mineralization events. The $\delta^{34}S_{pyrite}$ and $\Delta^{33}S_{pyrite}$ values for Oroya from location 2 overlap with both Fimiston pyrite and Hidden Secret HS1 vein pyrite. All show a prevalence of negative $\delta^{34}S_{pyrite}$ values and consistently low $\Delta^{33}S_{pyrite}$ values (Fig. 10B). The negative $\delta^{34}S_{pyrite}$ values in the Hidden Secret HS1 veins suggests that like Fimiston and Oroya mineralization, fluid fO_2 conditions at/or near the pyrite-hematite and pyrite-magnetite stability fields are recorded in Hidden Secret mineralization (Phillips et al. 1986; Clout 1989; Bateman and Hagemann 2004; Godefroy-Rodríguez et al., 2020a; Mueller et al. 2020a). The models of Phillips et al. (1986) and Evans et al. (2006) suggest that reduced metamorphic fluids may become oxidized due to local wall-rock interaction. Using empirical relationships in $\Delta^{33}S_{pyrite}$/$\delta^{34}S_{pyrite}$ data (see rock buffering trends in Fig. 10B), this study illustrates a contrary model as in both the Hidden Secret and Oroya mineralization types, there is evidence for a transition from variably negative $\delta^{34}S_{pyrite}$ values with low, mantle-like (~0 ± 0.1‰) $\Delta^{33}S_{pyrite}$ values to positive, restricted $\delta^{34}S_{pyrite}$ values (~0 to 5‰) with well-defined $\Delta^{33}S_{pyrite}$ MIF anomalies (> 0.1‰ or < -0.1‰). Based on the host rock and vein-hosted or disseminated settings of the samples, the trends in Fig. 10B are best explained by local wall-rock buffering of isotopically juvenile fluids (i.e., $\Delta^{33}S \sim 0‰$) by greenstone belt rocks and carbonaceous shales (e.g., Cox et al. 1991; Phillips et al. 1996; Mickuki 1998; Polito et al. 2001; Mueller 2020b; Mueller et al. 2020a). This buffering is inferred to lower fluid fO_2 from pyrite-hematite and pyrite-magnetite stable assemblages to

pyrite-stable and pyrrhotite-stable assemblages (Fig. 12). Multiple studies suggest that MIF $\Delta^{33}S$ anomalies in orogenic gold mineralization record recycled sulfur liberated during metamorphic devolatilization (Selvaraja et al. 2017; Laflamme et al. 2018; Groves et al. 2020). The results of this study emphasize an important caveat to this interpretation: $\Delta^{33}S$ MIF anomalies in ore-stage sulfides can be generated from the local interaction of hydrothermal fluids with wall rocks.

Conclusion

Both the Fimiston and Hidden Secret gold-telluride lodes developed as magmatic-hydrothermal gold events from a similar H_2O-CO_2-Au-Te-As-S-K-Rb-Ba fluid attendant with andesitic magmatism. The Fimiston and Hidden Secret lodes formed in ca. 2675 Ma D_{2b} transtensional architectures related to releasing bends along NW-striking master faults, namely, the Golden Mile and Towns faults, respectively. The Fimiston and Hidden Secret lodes were deformed during ca. 2660 Ma D_{2c} sinistral-reverse deformation, when Oroya mineralization developed from a relatively S-V-Au-Ag-Hg-Te-enriched fluid, and again from ca. 2650 to 2640 Ma when D_3 dextral faults and the Mt. Charlotte stockwork veins formed throughout the camp. Gold mineralization in the camp was punctuated from ca. 2675 to 2640 Ma. The majority of gold endowment reflects early, ca. 2675–2660 Ma magmatic-hydrothermal events (Fimiston/Hidden Secret + Oroya); however, the Mt. Charlotte stockwork veins likely record late metamorphic fluids which contributed to the earlier Au endowment.

Geochemical methods that aid in discriminating the Fimiston/Hidden Secret Au-Te mineralization event from the later Oroya Au-Te mineralization event include relative percentage changes in alteration mass balance calculations and correlation coefficients in LA-ICP-MS pyrite trace element data. These discriminatory geochemical methods quantify relative changes in alteration and trace metal systematics that seem to be inherent fingerprints of gold events. Sulfur isotope data ($\delta^{34}S_{pyrite}$, $\Delta^{33}S_{pyrite}$) does not contribute to discriminating the Fimiston/Hidden Secret Au-Te mineralization event from the later Oroya Au-Te mineralization event; rather, it highlights the effect of wall-rock buffering by ferrous greenstone belt rocks and carbonaceous shales on oxidized hydrothermal fluids. During the gold-telluride lode mineralization events, oxidized, juvenile magmatic fluids, represented by $\delta^{34}S_{pyrite} = \leq 0‰$ and $\Delta^{33}S_{pyrite} = \sim 0.0$ to 0.2‰, were buffered to $\delta^{34}S_{pyrite} = \sim 1$ to 5‰ and $\Delta^{33}S_{pyrite} = \sim 0.2$ to 0.7‰ by greenstone belt rocks and to $\delta^{34}S_{pyrite} = \sim 1$ to 5‰ and $\Delta^{33}S_{pyrite} = \sim \leq 0.3‰, \geq 0.7‰$ by interflow shales during the acquisition of locally sourced $\Delta^{33}S$ anomalies in ore-stage sulfides. These locally sourced $\Delta^{33}S$ anomalies in ore-stage sulfides emphasize that such anomalies may not record the involvement of recycled sulfur liberated during metamorphic devolatilization. Rather, $\Delta^{33}S$ anomalies in ore-stage sulfides can reflect variable fluid-rock interaction resulting from channelized or pervasive flow regimes within the mafic greenstone belt rocks and interflow shale horizons that comprise country rock near ore depositional sites.

Supplementary Information The online version contains supplementary material available at https://doi.org/10.1007/s00126-021-01077-w.

Acknowledgements We acknowledge Newmont Corporation and Kalgoorlie Consolidated Gold Mines for their support in this study. In particular, Matthew Baggott and Steve Turner have been instrumental in facilitating the study. Andreas Mueller and Gawen Jenkin are thanked for their constructive reviews, which significantly improved the quality of this manuscript.

Funding JM acknowledges additional funding provided by the Dean's Excellence in Science PhD scholarship at the University of Western Australia and a doctoral postgraduate scholarship provided by the Natural Sciences and Engineering Research Council of Canada. NT would like to acknowledge the support of the Hammond and Nisbet trust for its financial support.

References

Bateman R, Hageman S (2004) Gold mineralisation throughout about 45 Ma of Archaean orogenesis: protracted flux of gold in the Golden Mile, Yilgarn craton, Western Australia. Miner Deposita 39:536–559

Bateman R, Jones S (2015) Discussion: the timing of gold mineralization across the eastern Yilgarn Craton using U-Pb phosphate geochronology of hydrothermal minerals. Miner Deposita 50:885–888

Bateman R, Hagemann, SG, McCuaig TC, Swager, CP (2001a) Protracted gold mineralization throughout Archaean orogenesis in the Kalgoorlie camp, Yilgarn Craton, Western Australia: structural, mineralogical, and geochemical evolution: 4th International Archaean Symposium pp. 63–98

Bateman R, Costa S, Swe T, Lambert D (2001b) Archean mafic magmatism in the Kalgoorlie area of the Yilgarn Craton, Western Australia: a geochemical and Nd isotopic study of the petrogenetic and tectonic evolution of a greenstone belt. Precambrian Res 108:75–112

Bateman R, Ayer JA, Dubé B (2008) The Timmins-Porcupine Gold Camp, Ontario: anatomy of an Archean greenstone belt and ontogeny of gold mineralization. Econ Geol 103:1285–1307

Burrows DR, Spooner ETC (1987) Generation of a magmatic H_2O-CO_2 fluid enriched in Mo, Au, and W within an Archean sodic granodiorite stock, Mink Lake, Northwestern Ontario. Econ Geol 82:1931–1957

Cameron EM, Hattori K (1987) Archean gold mineralization and oxidized hydrothermal fluids. Econ Geol 82:1177–1191

Cameron EM (1988) Archean gold: relation to granulite formation and redox zoning in the crust. Geology 16:109–112

Claoué-Long JC, Compston W, Cowden A (1988) The age of Kambalda greenstone resolved by ion-microprobe: implications for Archaean dating methods. Earth and Planet Sci Lett 89:239–259

Clark ME (1980) Localization of gold, Mt Charlotte, Kalgoorlie, Western Australia. Unpublished B.Sc. (Hons) thesis, the University of Western Australia, 128 p

Clout JMF, Cleghorn JH, Eaton PC (1990) Geology of the Kalgoorlie gold field. Geology of the Mineral Deposits of Australia and Papua New Guinea (Hughes FE, Ed.), pp. 411–431

Clout JMF (1989) Structural and isotopic studies of the Golden Mile gold-telluride deposit, Kalgoorlie, Western Australia. Unpublished Ph.D. thesis, Monash University, 352 p

Colvine AC, Fyon JA, Heather KB, Marmont S, Smith PM, Troop DG (1988) Archean lode gold deposits in Ontario. Ontario Geological Survey Miscellaneous Paper 139, 210 p

Cox SF, Wall VJ, Etheridge MA, Potter TF (1991) Deformational and metamorphic processes in the formation of mesothermal vein-hosted gold deposits—examples from the Lachlan Fold Belt in central Victoria, Australia. Ore Geol Rev 6:391–423

Cox SF (2005) Coupling between deformation, fluid pressures, and fluid flow. In: Hedenquist JW, Thompson JFH, Goldfarb RJ, Richards JP (eds) Economic geology 100th anniversary volume, p 39–75

Doublier MP, Thébaud N, Wingate M, Romano S, Kirkland CL, Gessner K, Mole D, Evans N (2014) Structure and timing of Neoarchean gold mineralization in the Southern Cross district (Yilgarn Craton, Western Australia) suggest leading role of late Low-Ca I-type granite intrusions. J Struct Geol 26/B: 205–221

Dubé B, Mercier-Langevin P, Ayer J, Atkinson B, Monecke T (2017) Orogenic greenstone-hosted quartz-carbonate gold deposits of the Timmins-Porcupine camp, in Monecke T, Mercier-Langevin P, Dubé B, eds., Archean base and precious metal deposits, southern Abitibi greenstone belt, Canada. Reviews in Economic Geology19: 51–79

Eaton PC (1986) The regional geology of Kalgoorlie. Unpublished report to Kalgoorlie Mining Associates, 66 p

Evans KA, Phillips GN, Powell R (2006) Rock-buffering of auriferous fluids in altered rocks associated with the Golden Mile-style mineralization, Kalgoorlie gold field, Western Australia. Econ Geol 101:805–817

Farquhar J, Wing B (2003) Multiple sulfur isotopes and the evolution of the atmosphere. Earth Planet Sci Lett 213:1–13

Feldtmann FR (1916) The geology and ore deposits of Kalgoorlie, East Coolgardie Goldfield, part II. Geological Survey of Western Australia, Bulletin No. 69, 152 p

Fitzgerald M, Nixon DG (2016) The exploration and geology of the Hidden Secret Au-Ag lode orebody, Mount Charlotte, Kalgoorlie. Brownfields Exploration: Deep and Meaningful, pp. 16–20

Fletcher IR, Dunphy JM, Cassidy KF, Champion DC (2001) Compilation of SHRIMP U-Pb geochronological data, Yilgarn Craton, Western Australia, 2000–2001. Geoscience Australia Record 2001/47, 111 p

Gauthier L, Hagemann S, Robert F, Pickens, G (2004) New constraints on the architecture and timing of the giant Golden Mile deposit, Kalgoorlie, Western Australia. SEG 2004 Predictive Mineral Discovery Under Cover Abstract, pp. 353–356

Godefroy-Rodríguez M, Hagemann S, LaFlamme C, Fiorentini M (2020a) The multiple sulfur isotope architecture of the Golden Mile and Mount Charlotte deposits, Western Australia. Miner Deposita 55:797–822

Godefroy-Rodríguez M, Hagemann S, Frenzel M, Evans NJ (2020b) Laser ablation ICP-MS trace element systematics of hydrothermal pyrite in gold deposits of the Kalgoorlie district, Western Australia. Miner Deposita 55:823–844

Goldfarb RJ, Groves DI (2015) Orogenic gold: common or evolving fluid and metal sources through time. Lithos 233:2–26

Grant JA (1986) The isocon diagram—a simple solution to Gresens' equation for metasomatic alteration. Econ Geol 81:1976–1982

Groves DI, Goldfarb RJ, Santosh M (2016) The conjunction of factors that lead to the formation of giant gold provinces and deposits in non-arc settings. Geosci Front 7:303–314

Groves DI, Phillips GN (1987) The genesis and tectonic control on Archaean Gold Deposits of the Western Australian Shield—A metamorphic replacement model. Ore Geol Rev 2:287–322

Groves DI, Santosh M, Deng J, Wang Q, Yang L, Zhang L (2020) A holistic model for the origin of orogenic gold deposits and its implications for exploration. Miner Deposita 55:275–292

Gustafson JK, Miller FS (1937) Kalgoorlie geology re-interpreted. Econ Geol 32:285–317

Hagemann SG, Cassidy KF (2000) Archean orogenic lode gold deposits, in Hagemann SG, Brown PE (eds) Gold in 2000, Reviews in Economic Geology 14: 9–68

Hand JL (1998) Mineralised volcanic and sedimentary environments in the Eastern Goldfields. Unpublished Ph.D. thesis, Monash University, 403 p

Huston DL (1993) The effect of alteration and metamorphism on wall rocks to the Balcooma and Dry River South volcanic-hosted massive sulfide deposits, Queensland, Australia. J Geochem Explor 48:277–307

Hodkiewicz PF, Groves DI, Davidson GJ, Weinberg RF, Hagemann SG (2009) Influence of structural setting on sulphur isotopes in Archean orogenic gold deposits, Eastern Goldfields Province, Yilgarn, Western Australia. Miner Deposita 44:129–150

Hronsky JA, Groves DI, Loucks RR, Begg GC (2012) A unified model for gold mineralisation in accretionary orogens and implications for regional-scale exploration targeting methods. Miner Deposita 47:339–358

Ispolatov V, Lafrance B, Dubé B, Creaser R, Hamilton M (2008) Geologic and structural setting of gold mineralization in the Kirkland Lake-Larder Lake gold belt, Ontario. Econ Geol 103:1309–1340

Keats W (1987) Regional geology of the Kalgoorlie-Boulder gold-mining district: Geological Survey of Western Australia Report 21, 44 p

Kendrick MA, Honda M, Walshe J, Petersen K (2011) Fluid sources and the role of abiogenic-CH_4 in Archean gold mineralization. Constraints from noble gases and halogens. Precambrian Res 189:313–327

Kerr MJ, Hanley JJ, Kontak DJ, Morrison GG, Petrus J, Fayek M, Zajacz Z (2018) Evidence of upgrading of gold tenor in an orogenic quartz-carbonate vein system by late magmatic-hydrothermal fluids at the Madrid Deposit, Hope Bay Greenstone Belt, Nunavut Canada. Geochim Cosmochim Acta 241:180–218

Krapež B, Hand JL (2008) Late Archaean deep-marine volcaniclastic sedimentation in an arc-related basin: the Kalgoorlie Sequence of the Eastern Goldfields Superterrane, Yilgarn Craton, Western Australia. Precambrian Res 161:89–113

Krapež B, Brown SJA, Hand J, Barley ME, Cas RAF (2000) Age constraints on recycled crustal and supracrustal sources of Archaean metasedimentary sequences, Eastern Goldfields Province, Western Australia: evidence from SHRIMP zircon dating. Tectonophysics 322:89–133

Kent AJR, McDougall I (1995) ^{40}Ar-^{39}Ar and U-Pb age constraints on the timing of gold mineralization in the Kalgoorlie gold field, Western Australia. Econ Geol 90:845–849

LaFlamme C, Sugiono D, Thébaud N, Caruso S, Fiorentini M, Selvaraja V, Jeon H, Voute F, Martin L (2018) Multiple sulfur isotopes monitor fluid evolution of an Archean orogenic gold deposit. Geochim Cosmochim Acta 222:436–446

Large RR, Bull SW, Maslennikov VV (2011) A carbonaceous sedimentary source-rock model for Carlin-type and orogenic gold deposits. Econ Geol 106:331–358

Lawrence DM, Treloar PJ, Rankin AH, Boyce A, Harbidge P (2013) A fluid inclusion and stable isotope study at the Loulo mining

district, Mali, West Africa: implications for multifluid sources in the generation of orogenic gold deposits. Econ Geol 108:229–257

Lungan, A. 1986. The structural controls of the Oroya shoot: implications for the structure of the Kalgoorlie region, Western Australia: Unpublished B.Sc. (Hons) thesis, the University of Western Australia.

Masurel Q, Thébaud N, Allibone A, André-Mayer A-S, Hein KAA, Reisberg L, Bruguier O, Eglinger A, Miller J (2019) Intrusion-related affinity and orogenic gold overprint at the Paleoproterozoic Bonikro Ay-(Mo) deposit (Côte d'Ivoire, West African Craton). Miner Deposita. https://doi.org/10.1007/s00126-019-00888-2

McCuaig TC, Behn M, Stein H, Hagemann SG, McNaughton NJ, Cassidy KF, Champion D, Wyborn L (2001) The Boddington gold mine: a new style of Archean Au-Cu deposit [ext. abs.]. AGSO, Geoscience Australia Record 2001/37, p. 453–455

McDivitt JA, Lafrance B, Kontak DJ, Robichaud L (2017) The structural evolution of the Missanabie-Renabie gold district: pre-orogenic veins in an orogenic gold setting and their influence on the formation of hybrid deposits. Econ Geol 112:1959–1975

McDivitt JA, Kontak DJ, Lafrance B, Robichaud L (2018) Contrasting fluid chemistries, alteration characteristics, and metamorphic timing relationships recorded in hybridized orebodies of the Missanabie-Renabie gold district, Archean Wawa subprovince, Ontario, Canada. Econ Geol 113:397–420

McDivitt JA, Hagemann SG, Baggott MS, Perazzo S (2020) Geologic setting and gold mineralization of the Kalgoorlie gold camp, Yilgarn Craton, Western Australia. Geology of the world's major gold deposits and provinces, Sillitoe, R.H., Goldfarb, R.J., Robert, F., and Simmons, S.F., editors: Society of Economic Geologists Special Publication 23:251–274

McDivitt JA, Hagemann SG, Thébaud N, Martin LAJ, Rankenburg K (2021a). Deformation, magmatism, and sulfide mineralization in the Archean Golden Mile fault zone, Kalgoorlie gold camp, Western Australia. Econ Geol

McDivitt JA, Kontak DJ, Lafrance B, Petrus JA, Fayek M (2021b) A trace metal, stable isotope (H, O, S), and geochronological (U-Pb titanite) characterization of hybridized gold orebodies in the Missanabie-Renabie district, Wawa subprovince (Canada). Miner Deposita 56:561–582

McNaughton NJ, Mueller AG, Groves DI (2005) The age of the giant Golden Mile deposit, Kalgoorlie, Western Australia: ion-microprobe zircon and monazite U-Pb geochronology of a synmineralization lamprophyre dike. Econ Geol 100:1427–1440

Mernagh TP, Heinrich CA, Mikucki EJ (2004) Temperature gradients recorded by fluid inclusions and hydrothermal alteration at the Mount Charlotte gold deposit, Kalgoorlie, Australia. Can Mineral 42:1383–1403

Mikucki EJ (1998) Hydrothermal transport and depositional processes in Archean lode-gold systems: a review. Ore Geol Rev 13:307–321

Mueller AG, Muhling JR (2013) Silver-rich telluride mineralization at Mount Charlotte and Au-Ag zonation in the giant Golden Mile deposit, Kalgoorlie, Western Australia. Miner Deposita 48:295–311

Mueller AG, Muhling J (2020) Early pyrite and late telluride mineralization in vanadium-rich gold ore from the Oroya Shoot, Paringa South mine, Golden Mile, Kalgoorlie: 3. Ore mineralogy, Pb-Te (Au-Ag) melt inclusions, and stable isotope constraints on fluid sources. Miner Deposita 55:733–766

Mueller AG, Hagemann SG, Brugger J, Xing Y, Roberts MP (2020a) Early Fimiston and late Oroya Au-Te ore, Paringa South mine Golden Mile, Kalgoorlie: 4. Mineralogical and thermodynamic constraints on gold deposition by magmatic fluids at 420–300°C and 300 MPa. Miner Deposita 55:767–796

Mueller AG, Hagemann SG, McNaughton NJ (2020b) Neoarchean orogenic, magmatic and hydothermal events in the Kalgoorlie-Kambalda area, Western Australia: constraints on gold mineralization in the Boulder Lefroy-Golden Mile fault system. Miner Deposita 55:633–663

Mueller AG, Harris LB, Lungan A (1988) Structural control of greenstone-hosted gold mineralization by transcurrent shearing: a new interpretation of the Kalgoorlie Mining District, Western Australia. Ore Geol Rev 3:359–387

Mueller AG (2007) Copper-gold endoskarns and high-Mg monzodiorite-tonalite intrusions at Mt. Shea, Kalgoorlie, Australia: implications for the origin of gold-pyrite-tennantite mineralization in the Golden Mile. Miner Deposita 24:737–769

Mueller AG (2015) Structure, alteration, and geochemistry of the Charlotte quartz vein stockwork, Mt. Charlotte gold mine, Kalgoorlie, Australia: time constraints, down-plunge zonation, and fluid source. Miner Deposita 50:221–244

Mueller AG (2020a) Structural setting of Fimiston- and Oroya-style pyrite-telluride-gold lodes, Paringa South mine, Golden Mile, Kalgoorlie: 1. Shear zone systems, porphyry dikes and deposit-scale alteration zones. Miner Deposita 55:665–695

Mueller AG (2020b) Paragonite-chloritoid alteration in the Trafalgar Fault and Fimiston-and Oroya-style gold lodes in the Paringa South mine, Golden Mile, Kalgoorlie: 2. Muscovite-pyrite and silica-chlorite-telluride ore deposited by two superimposed hydrothermal systems. Miner Deposita 55:697–730

Nelson DR (1997) Evolution of the Archaean granite-greenstone terranes of the Eastern Goldfields, Western Australia: SHRIMP U-Pb zircon constraints. Precambrian Res 83:57–81

Nickel EG (1977) Mineralogy of the "Green Leader" gold ore at Kalgoorlie, Western Australia. Proc AusIMM 263:9–13

Parker H (2016) Fluid properties of the Hidden Secret lode in Kalgoorlie WA as determined by fluid inclusion analysis: Unpublished MSc thesis, Curtin University, 53p

Phillips GN, Groves DI (1983) The nature of Archaean gold-bearing fluids as deduced from gold deposits of Western Australia. J Geol Soc Aust 30:25–39

Phillips GN, Powell R (2010) Formation of gold deposits: a metamorphic devolatilization model. J Metamorph Geol 28:689–718

Phillips GN, Groves DI, Neall FB, Donnelly TH, Lambert IB (1986) Anomalous sulfur isotope compositions in the Golden Mile, Kalgoorlie. Econ Geol 81:2008–2015

Phillips GN, Groves DI, Brown IJ (1987) Source requirements for the Golden Mile, Kalgoorlie: significance to the metamorphic replacement model for Archean gold deposits. Can J Earth Sci 24:1643–1651

Phillips GN, Groves DI, Kerrich R (1996) Factors in the formation of the giant Kalgoorlie gold deposit. Ore Geol Rev 10:295–317

Phillips GN (1986) Geology and alteration in the Golden Mile, Kalgoorlie. Econ Geol 81:779–808

Polito PA, Bone Y, Clarke JDA, Mernagh TP (2001) Compositional zoning of fluid inclusions in the Archaean Junction gold deposit, Western Australia: a process of fluid – wall-rock interaction. Aust J Earth Sci 48:833–855

Radtke AS (1963) Data on cuprian coloradoite from Kalgoorlie, Western Australia. Econ Geol 58:593–598

Rasmussen B, Mueller AG, Fletcher IR (2009) Zirconolite and xenotime U-Pb age constraints on the emplacement of the Golden Mile Dolerite sill and gold mineralization at the Mt Charlotte mine, Eastern Goldfields Province, Yilgarn Craton, Western Australia. Contrib Mineral Petrol 157:559–572

Ridley J, Mengler F (2000) Lithological and structural controls on the form and setting of vein stockwork orebodies at the Mount Charlotte gold deposit, Kalgoorlie. Econ Geol 95:85–98

Robert F (2001) Syenite-associated disseminated gold deposits in the Abitibi greenstone belt, Canada. Miner Deposita 36:503–516

Robert F, Poulsen KH, Cassidy KF, Hodgson CJ (2005) Gold metallogeny of the Superior and Yilgarn cratons. Economic Geology 100th Anniversary Volume, pp. 1001–1033

Ross AA, Barley ME, Brown SJA, McNaughton NJ, Ridley JR, Fletcher IR (2004) Young porphyries, old zircons: new constraints on the timing of deformation and gold mineralization in the Eastern Goldfields from SHRIMP U-Pb zircon dating at the Kanowna Belle Gold Mine, Western Australia. Precambrian Res 128:105–142

Sellman L (2016) Hidden Secret: the characteristic mineralogy and geochemistry of a unique Ag-rich Au-Ag-Te Golden Mile deposit, Kalgoorlie, Western Australia: Unpublished B.Sc. (Hons) thesis, Curtin University, 144p

Selvaraja V, Caruso S, Fiorentini ML, LaFlamme CK, Bui T-H (2017) Atmospheric sulfur in orogenic gold deposits of the Archean Yilgarn Craton. Australia Geology 45(8):691–694

Sibson RH (1987) Earthquake rupturing as a mineralizing agent in hydrothermal systems. Geology 15:701–704

Sibson RH (2001) Seismogenic framework for hydrothermal transport and ore deposition: In Richards JP, Tosdal RM (eds.) Structural controls on ore genesis. Reviews in Economic Geology, v. 14, p. 25–50

Simpson ED, Gibson CG (1912) The geology and ore deposits of Kalgoorlie, East Coolgardie Goldfield part I: Geological Survey of Western Australia Bulletin No. 42, 168 p

Spooner ETC (1993) Magmatic sulphide/volatile interaction as a mechanism for producing chalcophile element enriched, Archean Au-quartz, epithermal Au-Ag and Au skarn hydrothermal ore fluids. Ore Geol Rev 7:359–379

Squire RJ, Allen CM, Cas RAF, Campbell IH, Blewett RS, Nemchin AA (2010) Two cycles of voluminous pyroclastic volcanism and sedimentation related to episodic granite emplacement during the late Archean: Eastern Yilgarn Craton, Western Australia. Precambrian Res 183:251–274

Sugiono D, Thebaud N, LaFlamme C, Fiorentini M, Martin L, Rogers J, Lorusso G, McFarlane C (2021) Integration of multiple sulfur isotopes with structural analysis unveils the evolution of ore fluids and source of sulfur at the Kanowna Belle Archean orogenic gold deposit, Yilgarn Craton, Western Australia. Miner Deposita. https://doi.org/10.1007/s00126-020-01032-1

Swager C (1989) Structure of Kalgoorlie greenstone—regional deformation history and implications for the structural setting of the Golden Mile gold deposits. Geological Survey of Western Australia Report No. 25, pp. 59–84

Thébaud N, Sugiono D, LaFlamme C, Miller J, Fisher L, Voute F, Tessalina S, Sonntag I, Fiorentini M (2018) Protracted and polyphased gold mineralisation in the Agnew District (Yilgarn Craton, Western Australia). Precambrian Res 310:291–304

Thébaud N, Allibone A, Masurel Q, Eglinger A, Davis J, André-Mayer AS, Miller J, Jessell M (2020) The Paleoproterozoic (Rhyacian) gold deposits of West Africa. Econ Geol

Tomich SA (1958) The Oroya shoot and its relationship to other flatly plunging ore pipes at Kalgoorlie. Technical Report No. 31 to Gold Mines of Kalgoorlie Ltd., 20 p

Tomkins AG (2010) Windows of metamorphic sulfur liberation in the crust: implications for gold deposit genesis. Geochim Cosmochim Acta 74:3246–3259

Travis GA, Woodall R, Bartram GD (1971) The geology of the Kalgoorlie goldfield. Special Publications Geological Society of Australia 3, pp. 175-190

Treagus SH (1983) A theory of finite strain variation through contrasting layers, and its bearing on cleavage refraction. J Struct Geol 5:351–368

Tripp GI (2013) Stratigraphy and structure in the Neoarchaean of the Kalgoorlie district, Australia: critical controls on greenstone-hosted gold deposits. Unpublished Ph.D. thesis, James Cook University, 476 p

Tripp GI (2014) How Neoarchean stratigraphy and structural geology determine the timing and controls of world-class greenstone gold camps in the Eastern Goldfields Province: key factors for gold exploration. Gold14@Kalgoorlie – Western Australia, p. 124–128

Valley JW (1986) Stable isotope geochemistry of metamorphic rocks. Rev Mineralogy and Geochem 16:445–489

Verbeeten A (2014) Petrographic thin section report on the hidden secret orebody. Unpublished report to Kalgoorlie Consolidated Gold Mines, 16 p

Vielreicher NM, Groves DI, Snee LW, Fletcher IR, McNaughton NJ (2010) Broad synchroneity of three gold mineralization styles in the Kalgoorlie gold field: SHRIMP, U-Pb, and $^{40}Ar/^{39}Ar$ geochronological evidence. Econ Geol 105:187–227

Vielreicher NM, Groves DI, McNaughton N, Fletcher I (2015a) The timing of gold mineralization across the eastern Yilgarn craton using U-Pb geochronology of hydrothermal phosphate minerals. Miner Deposita 50:391–428

Vielreicher NM, Groves DI, McNaughton N (2015b) Reply to discussion: the timing of gold mineralization across the eastern Yilgarn Craton using U-Pb geochronology of hydrothermal phosphate minerals. Mineral Deposita 50:889–894

Vielreicher NM, Groves DI, McNaughton N (2016) The Giant Kalgoorlie Gold Field Revisited. Geosci Front 7:359–374

Weinberg RF, Van de Borgh PV, Bateman RJ, Groves DI (2005) Kinematic history of the Boulder-Lefroy shear zone system and controls on associated gold mineralization, Yilgarn Craton, Western Australia. Econ Geol 100:1407–1426

Woodall RW (1965) Structure of the Kalgoorlie goldfield. 8th Commonweath Mining and Metallurgy Congress, Melbourne, pp. 71–79

Woods BK (1997) Petrogenesis and geochronology of felsic porphyry dykes in the Kalgoorlie Terrane, Kalgoorlie, Western Australia. Unpublished B.Sc. (Hons.) thesis, Curtin University, 154 p

Xing Y, Brugger J, Tomkins A, Shvarov Y (2019) Arsenic evolution as a tool for understanding formation of pyritic gold ores. Geology 47:335–338

Xue Y, Campbell I, Ireland TR, Holden P, Armstrong R (2013) No mass-independent sulfur isotope fractionation in auriferous fluids supports a magmatic origin for Archean gold deposits. Geology 41:791–794

Yeats CJ, McNaughton NJ, Ruettger D, Bateman R, Groves DI, Harris JL, Kohler E (1999) Evidence for diachronous Archean lode gold mineralization in the Yilgarn Craton, Western Australia: a SHRIMP U-Pb study of intrusive rocks. Econ Geol 94:1259–1276